IMPROVEMENT IN PHOTOCATALYTIC ACTIVITY OF STABLE WO$_3$ NANOPLATELET GLOBULAR CLUSTERS ARRANGED IN A TREE-LIKE FASHION: INFLUENCE OF ROTATION VELOCITY DURING ANODIZATION

Fernández-Domene, R.M.[a]; Sánchez-Tovar, R.[a]; Lucas-Granados, B. [a] García-Antón, J.[a]*

[a]*Ingeniería Electroquímica y Corrosión (IEC). Departamento de Ingeniería Química y Nuclear. ETSI Industriales. Universitat Politècnica de València. Camino de Vera s/n,*

46022 Valencia, Spain.

Tel. 34-96-387 76 32, Fax. 34-96-387 76 39, e-mail: jgarciaa@iqn.upv.es

This study investigates the influence of controlled hydrodynamic conditions during anodization of tungsten (W) on the morphological, electrochemical and photocatalytic properties of a novel WO$_3$ nanostructure: globular clusters of nanoplatelets associated in a tree-like fashion. For this purpose different techniques such as Field-Emission Scanning Electronic Microscopy (FE-SEM), electrochemical impedance spectroscopy (EIS) measurements, Mott-Schottky (M-S) analysis and photoelectrochemical water splitting tests have been carried out. Photoanodes obtained at 375 rpm showed the best photoresponse, much higher than that of conventional WO$_3$ nanoplatelets, which can be ascribed to a noteworthy increase in the electrochemically active surface area leading to improved charge transfer at the interface. Moreover, the improved WO$_3$ nanostructure displayed very good long-term photostability when irradiated with AM 1.5 illumination, thus solving the recurrent problem of the poor stability of WO$_3$ against photodegradation processes.

KEYWORDS: WO$_3$ nanostructures; anodization; hydrodynamic conditions; photocatalytic activity; water splitting.

1. INTRODUCTION

Semiconducting metal oxides, such as TiO_2 [1-3], WO_3 [4-10], Fe_2O_3 [11, 12] or ZnO [13, 14], are being widely investigated for their use as photoanodes due to the wide range of properties they can offer. Among the key functional properties that these oxides must have for photoelectrochemical processes, the resistance to degradation in the required environments (chemical dissolution, electrochemical corrosion, photocorrosion and other light-driven degradation processes) is of critical importance [15, 16]. Therefore, when using a photoelectrode, it is essential to assure that it is resistant to degradation and that its photoelectrochemical response is stable with time.

On the other hand, tungsten trioxide (WO_3) has generated great interest in the last years due to its numerous applications in electrochromic devices, gas sensors, photoelectrochemical water splitting or photodegradation of organic compounds [6-8, 10, 17-27]. To increase the efficiency of the WO_3-based photoanodes, nanostructured electrodes (such as nanotubes, nanorods/nanowires, nanoplatelets or nanoflakes) are required to provide a high specific surface area [4-10, 18-20, 22-31]. Although WO_3 is resistant to chemical attack in acidic media [26, 32-34], its stability under illumination is not good in numerous electrolytes, even in strong acid solutions, which has been manifested in many works as a decay of the initial photocurrent density with time upon illumination [30, 35-38].

In a recent paper [39] we presented a novel WO_3 nanostructure with very high surface area formed by tree-like nanoplatelets clusters. This innovative nanostructure was synthesized by anodization in sulfuric acid media in the presence of fluoride anions and

under controlled hydrodynamic conditions using a rotating disc electrode (RDE), and its photoresponse was very high compared with that of samples synthesized under stagnant conditions. Although the new nanostructure formed under hydrodynamic conditions presented larger surface areas and provided higher photocurrent densities than that formed at 0 rpm, it was also observed that at high rotation velocities (2000 rpm) the thickness of the nanoplatelet layer, and hence the surface area exposed to the electrolyte, was significantly lower than at lower rotation velocities (500 rpm). This fact indicated that the influence of hydrodynamic conditions on the formation and growth of the new tree-like nanostructure was not linear, and further study was necessary to investigate the mechanism of formation of these WO_3 nanoplatelets clusters.

The objectives of the present study are, therefore: (1) to optimize the dimensions and photoactivity of the tree-like nanoplatelets by modifying the rotation velocity of the RDE and (2) to find optimal conditions to assure that the new nanostructure does not undergo degradation under illumination, that is, its photoresponse remains stable with time. To accomplish both objectives, different techniques have been used, such as Field-Emission Scanning Electronic Microscopy (FE-SEM), electrochemical impedance spectroscopy (EIS), Mott-Schottky (M-S) analysis and photoelectrochemical measurements.

2. EXPERIMENTAL PROCEDURE

Tungsten samples were teflon-coated cylindrical bars of 8 mm in diameter. Before anodization, samples were abraded using 220, 500, 1000 and 4000 grit SiC papers to

remove scratches and other imperfections from the surface. Then, the samples were sonicated in ethanol for 2 min and dried in a N_2 stream. Anodization of tungsten samples was carried out in a 1.5M H_2SO_4 + 0.1M NaF electrolyte, at 20V and 50 ºC for 4 hours, under controlled hydrodynamic conditions (from 0 to 1000 rpm) by using a rotating disc electrode (RDE) and a platinum mesh as cathode. The area of the working electrode (tungsten sample) exposed to the electrolyte was 0.5 cm^2. After anodization, samples were annealed at 400 ºC for 4 hours in the presence of oxygen. The morphology of the formed nanostructures was characterized by Field Emission Scanning Electron Microscopy (FE-SEM).

Electrochemical measurements (electrochemical impedance spectroscopy (EIS) and Mott-Schottky analysis) were performed under dark conditions in a 1M HCl electrolyte. An Ag/AgCl (3 M KCl) electrode was the reference electrode, and a platinum tip was the counter electrode. The illuminated area of the working electrode exposed to the electrolyte was 0.13 cm^2. For EIS measurements at open circuit potential, the potential perturbation amplitude was 10 mV, in the frequency range of 10 kHz to 10 mHz. Mott-Schottky plots were determined at a constant frequency of 5 kHz using a 10 mV amplitude signal and scanning the potential from a value of 0.5 $V_{Ag/AgCl}$ in the negative direction at a rate of 50 mV s^{-1}.

Photocurrent density-potential curves and stability tests were carried out in many different electrolytes using an Autolab PGSTAT302N potentiostat under simulated sunlight illumination AM 1.5 (100 mW cm^2), with the purpose of finding an electrolyte where the WO_3 samples were stable. The electrochemical cell was the same as that described above for the electrochemical measurements. Photocurrent density-potential

curves were recorded by scanning the potential from −0.24 V to 1.02 V with a scan rate of 2 mV s^{-1}, switching the light on and off (60 s in the dark and 20 s in the light) to obtain in the same measurement photocurrent and dark current values. Afterwards, a potential of 1.02 V was kept constant for 1 hour under illumination to evaluate the samples stability. Additionally, the indirect band-gap energy of the samples was determined measuring the photocurrent density spectrum at 1.02 $V_{Ag/AgCl}$ in the wavelength range from 300 to 500 nm, in a 1M HCl electrolyte.

3. RESULTS AND DISCUSSION

3.1. Morphological characterization (FE-SEM)

Figure 1 shows the FE-SEM images of the samples anodized in the 1.5M H_2SO_4/0.1M NaF solution at different rotation velocities. It can be observed that in all cases, the nanostructures formed on the W surface presented nanoplatelet morphology, as other authors reported when anodizing in similar acid electrolytes [18, 20, 25, 29, 39, 40]. However, the dimensions and morphology of these nanoplatelets were influenced by hydrodynamic conditions. At 0 rpm (**Figure 1a**), nanoplatelets grew quite orderly and almost orthogonal to the electrode surface. The nanoplatelets layer was crisscrossed by numerous cracks and at least another nanoplatelets layer could be observed underneath the first one. At 125 rpm (**Figure 1b**), nanoplatelets started forming globular clusters, although most of these clusters still grew forming a single-level layer; in this case, several cracks were also observed on the WO_3 layer. At rotation velocities higher than 125 rpm (**Figures 1c to 1g**), nanoplatelets globular clusters grew in a tree-like manner, forming a multilevel WO_3 layer resembling a coniferous forest or a coral reef seen from

above and thus exposing more surface area to the electrolyte. It can be observed that at high rotation velocities (**Figures 1e to 1g**) these nanoplatelet clusters were denser than at lower rpm, although their size did not vary appreciably with the rotation velocity. **Figure 2a** plots the total thickness of the nanoplatelets layer and the % of surface covered by these nanostructures as a function of the rotation velocity. The total thickness was obtained from FE-SEM cross-sectional images. **Figure 2b** shows, as an example, the FE-SEM cross-sectional images of the samples anodized under 0 and 500 rpm. It can be seen that the thickness of the WO_3 nanoplatelets layer increased with increasing rpm until reaching a maximum value at 375 rpm, and then decreased again. Concerning the % of surface coverage, it decreased more or less linearly with rotation velocity. These differences in dimensions and surface coverage will be discussed in the next section when studying the current density transients recorded during the anodization process.

*3.2. Influence of rotation velocity on the anodization process*

In order to understand the influence of rotation velocity on the formation and growth of WO_3 nanoplatelets, current density transients recorded during the anodization of the W samples are presented in **Figure 3**. A notable decrease in current density can be observed during the first seconds of anodization, regardless of the rotation velocity. This decrease is associated with the formation of a compact WO_3 layer on the electrode surface [4, 39, 41], according to:

$$W + 3H_2O \rightarrow WO_3 + 6H^+ + 6e^- \tag{1}$$
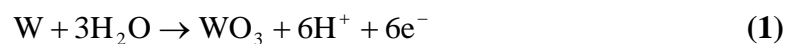
Subsequently, current density started increasing, indicating the dissolution of the WO_3 layer due to the effect of H^+ [24, 29, 39, 42] and F^- [24, 39, 41]. This dissolution process resulted in the release of soluble species from the electrode surface:

$$WO_3 + 2H^+ \rightarrow WO_2^{2+} + 2H_2O \tag{2}$$

$$WO_3 + 6H^+ + nF^- \rightarrow \left[WF_n\right]^{(n-6)} + 3H_2O \tag{3}$$
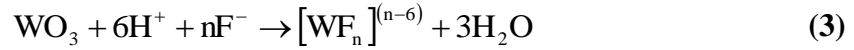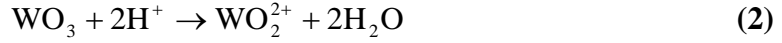
Afterwards, current density gradually decreased again, eventually reaching a steady-state value. This decrease and the later stabilization of current density can be explained by the precipitation of soluble species upon reaching supersaturation conditions near the electrode surface. This precipitation in the form of nanoplatelets took place according to the following reactions [24, 29, 39, 42]:

$$WO_2^{2+} + 2H_2O \rightarrow WO_3 \cdot H_2O + 2H^+ \tag{4}$$

$$WO_2^{2+} + 3H_2O \rightarrow WO_3 \cdot 2H_2O + 2H^+ \tag{5}$$
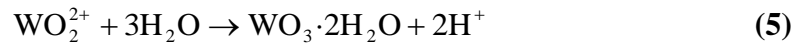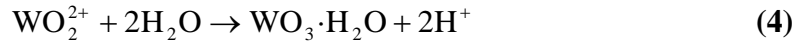
In a previous work is was demonstrated through Raman spectroscopy that the main constituent of the hydrated WO_3 nanoplatelets was $WO_3 \cdot 2H_2O$, although the presence of some $WO_3 \cdot H_2O$ was also detected [39]. After annealing the samples at 400 ºC for 4 hours, crystalline monoclinic WO_3 was obtained [39].

Under static conditions (0 rpm), current densities recorded during the whole anodization process were notably lower than under hydrodynamic conditions. Moreover, steady-state values were attained much earlier than with rotation, indicating that the WO_3

nanoplatelet layer completely covered the electrode surface after ~2000 s from the beginning of the anodization process.

As the rotation velocity increased, current density values associated with the dissolution of the initial WO_3 layer also increased. This fact is explained by taking into account the velocity profile of the electrolyte near the RDE. When the RDE rotates, the solution is drawn up from the bulk electrolyte towards the electrode along the axis normal to the surface, and afterwards, due to the centrifugal force, it is expelled towards the outer edge of the electrode. The expression for the fluid velocity in the normal direction, v_y, is [43]:

$$v_y = -0.51\omega^{3/2}v^{-1/2}y^2 \tag{6}$$

where ω is the angular velocity, v the kinematic viscosity of the fluid, and y (in cylindrical coordinates) the distance from the electrode surface in the normal direction.

Eq. (6) implies that v_y increases (in absolute value) with increasing the rotation velocity (ω). Hence, faster electrode rotation permitted the ions in the electrolyte (F^- and H^+) to transport to the electrode more rapidly (both by convection and by diffusion through the stagnant layer), resulting in higher current densities being measured at the working electrode due to the enhancement of the WO_3 dissolution (eqs. (2) and (3)), and the subsequent exposure of the W bare surface to the electrolyte, which oxidized again (eq. (1)). Consequently, an increase in the rotation velocity increased the release of soluble species from the electrode surface, which would result in a higher precipitation rate of hydrated WO_3 in the form of nanoplatelets (eqs. (4) y (5)) due to supersaturation conditions being reached earlier than at low ω. However, it was observed before from

8

the FE-SEM images that the thickness of the WO_3 nanoplatelets layer, as well as the degree of surface covered by them, were smaller at high rotation velocities (**Figure 2**). This is explained by the existence of a radial flow because of the centrifugal force that threw the electrolyte outwards from the center of the electrode, with the fluid velocity increasing towards the edge of the disc with increasing distance from the rotation axis in the radial direction (r) and ω, according to [43]:

$$\upsilon_r = 0.51\omega^{3/2}v^{-1/2}ry \tag{7}$$

Consequently, soluble species near the electrode surface were constantly swept away radially at a velocity directly dependent on the rotation velocity and the radius. As described above, for nanoplatelets to precipitate on the electrode surface, soluble species must reach a supersaturation concentration near the electrode. As ω increased, this critical concentration was more difficult to accomplish, especially at high values of r.

Therefore, hydrodynamic conditions influenced the growth of nanoplalets in two opposite ways: on the one hand, hydrodynamic conditions enhanced mass transfer towards the electrode surface, thus favoring the formation of soluble species responsible for the formation of nanoplatelets; on the other hand, mechanical convection reduced the concentration of soluble species close to the electrode surface, hence decreasing the nanoplatelets growth rate by precipitation [5, 29, 39]. In this case, according to the FE-SEM images and the nanoplatelet layer thicknesses shown in **Figure 2**, the first factor (enhancement of mass transfer, soluble species formation and subsequent precipitation) had more influence at low rotation velocities (up to 375 rpm), while at rotation velocities higher than 375 rpm it was the second factor (decrease of soluble species

concentration near the surface) that predominated over the first one in determining the formation and growth of nanoplatelets, since the thickness of the nanoplatelets layer decreased at high rpm.

Current densities recorded at the end of the 4-hours anodization process also increased with increasing rotation velocity. These values represent an approximately steady-state between the dissolution of the WO_3 layer (eq. (1)) and the precipitation of soluble species to hydrated WO_3 in the form of nanoplatelets (eqs. (4) and (5)). Hence, an increase in steady-state current density with ω implies that the degree of surface coverage was smaller at high ω, which is also consistent with the previous results (**Figure 2**).

3.3. Electrochemical characterization

The electrochemical characterization of the WO_3 nanostructures/electrolyte interface was performed in the dark through EIS measurements and Mott-Schottky analysis.

Figure 4 shows the Nyquist and Bode-phase diagrams for all the samples, anodized at different rotation velocities. Nyquist plots (**Figure 4a**) exhibit one or two unfinished semicircles, depending on the rotation velocity, and relatively low impedance values. At 0 and 125 rpm, two semicircles can be discerned, one at intermediate frequencies and the other at low frequencies (inset in **Figure 4a**), which correspond with the two peaks that appear in the Bode-phase plots (**Figure 4b**). At 500 rpm and higher rotation velocities (750 and 1000 rpm), only one semicircle can be discerned from Nyquist plots, in accordance with the peak observed in the phase angle. At 250 and 375 rpm, a single

semicircle is appreciable in Nyquist plots, but two time constants can be detected from the Bode-phase plots. The first semicircle observed in the Nyquist plots at 0 and 125 rpm has a considerably lower amplitude than the second semicircle, being the amplitude of the latter more similar to that of the single semicircle observed at higher rotation velocities. Therefore, this first time constant can be associated with some surface effects related to the specific morphology of the samples anodized at low rotation velocities, especially at 0 and 125 rpm. At 0 rpm, the morphology of the WO_3 nanostructures was observed to be vertically-alligned nanoplatelets, while at 125 rpm this morphology slightly changed and single nanoplatelets started forming globular clusters, but in both cases nanoplatelets formed a single-level layer (**Figure 1**). As rotation velocity increased, globular clusters of nanoplatelets began forming multilevel layers, and this first time constant was not so clearly observed from EIS plots (at 250 and 375 rpm, where a transition ocurred) or simply disappeared (500, 750 and 1000 rpm). The second time constant, which is common for all the samples, can consequently be associated with the charge-transfer resistance and the double layer capacitance of the WO_3 nanostructures.

Since the impedance response of the samples, especially the variation of the phase angle with frequency, was observed to change depending on the rotation velocity used during anodization, EIS experimental data have been fitted to the electrical equivalent circuits shown in **Figure 5a** (from 0 to 375 rpm) and in **Figure 5b** (from 500 to 1000 rpm). In these circuits, R_S is the electrolyte resistance; the R_1-CPE_1 time constant is associated with some surface effects due to the morphology of the nanoplatelet layer formed at 0 and low rpm values (mainly 125 rpm), while the R_{nano}-CPE_{nano} time constant is related to the charge transfer between the WO_3 nanostructure and the electrolyte. Constant

Phase Elements (CPEs) have been used instead of pure capacitors, to account for the non-ideality of the system under measurement. The impedance of a constant-phase element is defined as:

$$Q = Z_{CPE} = \left[C(j\omega)^n\right]^{-1} \tag{8}$$

where n, defined as a CPE power, is an adjustable parameter that lies between -1 and 1. For $n = 1$ the CPE describes an ideal capacitor, and for $n = 0$ the CPE is an ideal resistor. For $0.5 < n < 1$ the CPE describes a frequency dispersion of time constants due to local heterogeneities in the dielectric material. A pure inductance yields $n = -1$.

CPEs of the WO_3 nanostructures have been converted into pure capacitances, C, by using the following equation [44, 45]:

$$C_{nano} = \frac{(Q_{nano} \cdot R)^{1/\alpha}}{R} \tag{9}$$

where Q_{nano} is the impedance of the CPE_{nano}. For the equivalent circuit shown in **Figure 5a**, $R = R_{nano}$, while for the equivalent circuit in **Figure 5b**, $R = \left(\frac{R_S \cdot R_{nano}}{R_S + R_{nano}}\right)$ [44, 45].

The values of R_{nano} and C_{nano} have been plotted against the rotation velocity in **Figure 6**. A clear correlation between both values is evident: high R_{nano} values imply low C_{nano} values, and vice versa. At 0 and 125 rpm, both parameters were similar, but as rotation velocity increased (up to 500 rpm), R_{nano} decreased and C_{nano} increased. This fact can be

explained by an increase in the surface area exposed to the electrolyte, which increased the double layer capacitance and reduced the charge-transfer resistance at the nanostructure/electrolyte interface [41] due to a large number of electrochemically active sites being permeated by the electrolyte [8]. At higher rotation velocities, R_{nano} increased again whereas C_{nano} decreased. Although the morphology of the WO$_3$ nanostructures formed at 750 and 1000 rpm was similar than that obtained at lower rpm (**Figure 1**), nanoplatelets clusters formed at high rotation velocities were observed to grow in a more compact manner and, besides, the thickness of the WO$_3$ nanoplatelet layer was lower for these samples (**Figure 2**), which resulted in a decrease of the active surface area exposed to the electrolyte. These factors led to a reduction in the efficiency of electron transport [30] and, therefore, the charge-transfer resistance increased and the double layer capacitance decreased at 750 and 1000 rpm.

In order to investigate the semiconducting properties of the WO$_3$ nanoplatelets layer, the electrochemical interfacial capacitance was measured as a function of the applied potential. Mott-Schottky (M-S) analysis was performed to obtain the donor density, N_D, and the flat-band potential, U_{FB}, of the nanostructures formed at different rotation velocities. **Figure 7** shows the Mott-Schottky plots of the different samples. The positive slopes of these M-S plots are characteristic of *n*-type semiconductors, and the nanostructure/electrolyte interface can be described by the corresponding Mott-Schottky equation:

$$\frac{1}{C^2} = \frac{1}{C_H^2} + \frac{2}{\varepsilon_r \varepsilon_0 e N_D}\left(U - U_{FB} - \frac{kT}{e}\right) \qquad \textbf{(10)}$$

where C is the measured interfacial capacitance, C_H is the capacitance of the Helmholtz layer, ε_r is the relative permittivity or dielectric constant of the WO$_3$ nanostructures (a value of 50 has been assumed for the WO$_3$ [9, 22, 35, 36]), ε_0 is the vacuum permittivity ($8.85 \cdot 10^{-14}$ F/cm), e is the electron charge ($1.60 \cdot 10^{-19}$ C), U is the applied potential, k is the Boltzmann constant ($1.38 \cdot 10^{-23}$ J/K) and T is the absolute temperature.

Values of N_D and U_{FB} can be determined from the slope and the intercept, respectively, of a linear representation between C^{-2} and U, according to eq. (10). It is noteworthy that C_H does not influence the value of N_D, but it affects the value of U_{FB}. It is usually assumed that the Helmholtz layer capacitance is so large compared with the space charge layer capacitance that the total capacitance measured can be treated as the space charge layer capacitance and the potential drop caused by the applied potential occurs entirely within the space charge region. However, in highly doped semiconductors (such as nanostructured metal oxides), C_H should not be neglected, since a significant part of the potential difference at the semiconductor/electrolyte interface extends to the Helmholtz layer in the solution [46-48]. Therefore, in the present study, C_H values have not been neglected. For practical purposes, since the electrolyte used in electrochemical measurements (1M HCl) was sufficiently concentrated, the capacitance response of the Guoy-Chapman diffuse layer can be ignored, so $C_H \approx C_{nano}$.

Table 1 shows the values of N_D and U_{FB} for the WO$_3$ nanostructures synthesized at different rotation velocities. As mentioned above, U_{FB} values have been determined by taking into account the capacitance of the Helmholt layer in eq. (10). It can be seen that N_D were very high, of the same order of magnitude than values reported in the literature for WO$_3$ nanoplatelets, nanoparticles and nanorods [9, 22, 35, 36, 49]. Samples

anodized at 250, 375 and 500 rpm presented significantly higher donor densities than the rest of the samples, which can be explained by an increase of the interfacial capacitance due to the larger surface area exposed to the electrolyte for the samples anodized at intermediate rotation velocities, resulting in higher concentration of oxygen vacancies. These results are consistent with the increase in C_{nano} and the decrease in R_{nano} (increase in the nanostructures conductivity) observed above for these samples (**Figure 6**). Concerning the U_{FB}, there was no clear tendency with rotation velocity, and values varied within a small range from 0.23 to 0.30 $V_{Ag/AgCl}$, similar to values obtained by other authors [22, 35, 36].

3.4. Degradation resistance of the samples

As it has been mentioned in the introduction section, resistance to degradation in a given environment under illumination is a critical requirement for the photoanode material. The first step is to ensure that the semiconductor oxide used as photoanode does not undergo chemical and electrochemical degradation in the dark. In general, it is not recommended to work with WO_3 at pH higher than 4-5, since it is thermodynamically unstable and dissolves [33, 34]. **Figure 8a** shows the photocurrent density-potential (i_{ph}-U) curves for the sample anodized at 500 rpm, recorded in different electrolytes with different pH values. The sample synthesized at 500 rpm has been used throughout this section by way of illustration, and the conclusions obtained here can be perfectly extrapolated to the rest of the samples. It can be observed that the shape of the photocurrent density response of samples tested in 0.1M Na_2SO_4 and 0.1M H_2SO_4 solutions was similar, although in the latter case, photocurrent density values were higher at potentials $U > 0.8$ V, while dark current densities were similar at these

potentials. In both cases, dark current densities were stable and very low (of the order of few μA cm^{-2} or even lower). These results denote that WO_3 nanostructures were resistant to chemical and electrochemical degradation under dark conditions in the 0.1M Na_2SO_4 and 0.1M H_2SO_4 electrolytes, especially in the acidic one.

On the other hand, the photocurrent density-potential curve recorded in 0.1M KOH is completely different. Although the curve was also obtained under chopped illumination, it was difficult to distinguish between photocurrent and dark current densities (**Figure 8a**). The appearance of a wide peak centered at ~0.5V indicates that some kind of transformation in the characteristics or composition of the WO_3 surface film took place. Moreover, after the photoelectrochemical test, the WO_3 nanostructure was completely dissolved from the surface in contact with the KOH electrolyte. These results imply that WO_3 nanoplatelets were unstable in alkaline media, as expected, due to the OH^--induced chemical dissolution, in accordance with [32, 34, 49]:

$$WO_3(s) + OH^- \rightarrow WO_4^{2-}(aq) + H^+ \tag{11}$$
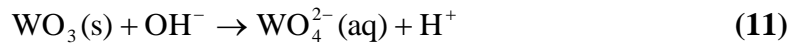
According to Anik and Cansizoglu [32], the chemical dissolution of the oxide film given in eq. (11) is the rate-determining step in the oxidation of W to WO_3. This fact can explain the very high current densities obtained in the 0.1M KOH electrolyte, which correspond to the active oxidation of the W substrate.

Concerning the photostability of the WO_3 nanostructures synthesized at 500 rpm, **Figure 8b** shows the photocurrent density transients obtained at an applied potential of 1.02 V in the 0.1M Na_2SO_4 and 0.1M H_2SO_4 electrolytes. It can be observed that

photocurrent density values considerably decreased after 1 hour of exposition to simulated sunlight, regardless of the electrolyte: a decrease of 83.9% (from 0.56 to 0.09 mA cm^{-2}) was observed in the case of the 0.1M Na$_2$SO$_4$ solution, and a decrease of 81.1% (from 1.11 to 0.21 mA cm^{-2}) the 0.1M H$_2$SO$_4$ electrolyte. Other authors observed a similar drop in photocurrent densities with time working with WO$_3$ photoanodes in acidic or neutral electrolytes [30, 35-38, 49, 50].

Although it has been demonstrated that WO$_3$ nanoplatelets were chemical and electrochemically stable in the acidic and neuter solutions, the fast decrease in photocurrent densities with time in these electrolytes indicates that samples underwent degradation under illumination. Photocorrosion is a phenomenon that takes place when the photogenerated holes in the valence band oxidize the semiconductor itself, instead of species present in the electrolyte [16, 51]. In the case of WO$_3$, photocorrosion reaction proceeds through the following reaction:

$$2WO_3 + 12h^+ \rightleftharpoons 2W_{(aq)}^{6+} + 3O_2 \tag{12}$$
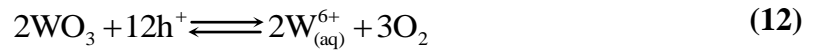
Moreover, if holes accumulate near the semiconductor surface instead of reacting with species in the electrolyte, photocurrent density can also decrease with time due to the recombination of part of the photogenerated charge carriers (electrons and holes) [52]. A solution for these two issues (photocorrosion and recombination) can be the addition of a hole scavenger (electron donor) to the electrolyte, such as methanol [8, 9, 53]. The hole scavenger reacts with the holes at the semiconductor/electrolyte interface, thus reducing the complications arising from hole accumulation. **Figure 9a** shows the photocurrent density-potential curve for the sample anodized at 500 rpm, recorded in a

0.1M H_2SO_4 electrolyte in the absence and presence of 1M methanol. An increase in photocurrent density values can be clearly observed in the 0.1M H_2SO_4 + 1M CH_3OH solution, which indicates hole scavenging by CH_3OH [8, 9, 53], according to the following reaction [53, 54]:
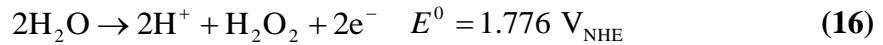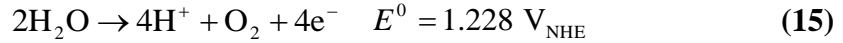
$$CH_3OH(ads) + h^+ \rightarrow \, ^{\bullet}CH_2OH(ads) + H^+ \qquad \textbf{(13)}$$
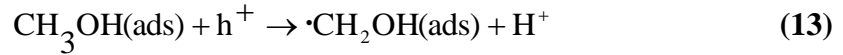
Besides, the adsorbed intermediate radical $^{\bullet}CH_2OH(ads)$, generated during the oxidation of methanol, can also effectively inject an additional electron into the conduction band of WO_3:

$$^{\bullet}CH_2OH(ads) \rightarrow CH_2O(ads) + H^+ + e_{cb}^- \qquad \textbf{(14)}$$
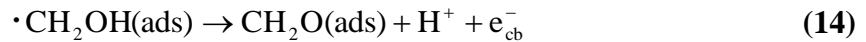
which explains the important increase observed in photocurrent density in the presence of CH_3OH [8, 9, 53]. However, these high photocurrent density values recorded in the presence of CH_3OH tended to gradually decrease with increasing irradiation time, as in the case of the electrolyte without methanol (**Figure 9b**). In this case, the photocurrent density decrease was of 54.6% (from 1.74 to 0.79 mA cm^{-2}) in one hour. Although this photocurrent density drop is lower than that recorded in the 0.1M H_2SO_4 solution, this result demonstrates that neither photocorrosion due to hole accumulation at the interface nor recombination of photogenerated electron-hole pairs were the main cause of the fast photocurrent density decrease with time under simulated sunlight.

The rapid deactivation of the WO_3 electrodes upon illumination must be ascribed to a different light-driven degradation mechanism. Several authors have reported the

occurrence of photocorrosion of WO_3 induced by the formation of H_2O_2 during incomplete water oxidation (a reaction that is kinetically favored over oxygen evolution reaction (OER) in WO_3 photoanodes under illumination, in spite of being thermodynamically less feasible [34, 37, 55-58]):

$$2H_2O \rightarrow 4H^+ + O_2 + 4e^- \quad E^0 = 1.228 \text{ V}_{NHE} \tag{15}$$

$$2H_2O \rightarrow 2H^+ + H_2O_2 + 2e^- \quad E^0 = 1.776 \text{ V}_{NHE} \tag{16}$$

Subsequently, hydrogen peroxide interacts with the WO_3 nanostructure, and peroxo-species accumulates on the surface, partially blocking it and thus reducing photoactivity [26, 37, 38, 53]. These tungsten peroxide species can also induce the recombination of photogenerated electron-hole pairs at the surface of the WO_3 nanostructures [38]. Hydroxyl radicals may form during the process, as well [57]:

$$H_2O \rightarrow \cdot OH + H^+ + e^- \quad E^0 = 2.85 \text{ V}_{NHE} \tag{17}$$
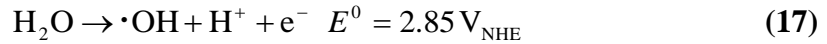
which can subsequently interact with the WO_3 surface [36, 57], leading to the same negative consequences for the photoanode stability.

On the other hand, the oxidation of some acid counteranions (Cl^-, SO_4^{2-}, $CH_3SO_3^-$, etc.) can also take place on the photoanode surface under illumination, since holes in the valence band of WO_3 have a potential of ~2.97 V_{HNE} at pH 0 [56, 57, 59], enough to drive these oxidation reactions ($E^0(Cl_2/Cl^-) = 1.358V_{NHE}$; $E^0(S_2O_8^{2-}/SO_4^{2-}) = 2.010V_{NHE}$ $E^0((CH_3SO_3)_2/CH_3SO_3^-) = 2.12V_{NHE}$ [60]). Hence, the oxidation of acid counteranions can kinetically compete with peroxide formation and OER [34, 56, 57, 60].

Hill and Choi [56] observed that the oxidation of chloride anions was the dominant photooxidation reaction taking place on the WO_3 surface when immersing the photoanode in a 0.1M NaCl solution (pH 1-5) under illumination. They also observed that photocurrent density values did not significantly decrease over time, which they ascribed to the effective suppression of peroxide formation by chloride oxidation. On the other hand, Augustynski and co-workers recently reported a very good photoelectrochemical behavior of nanostructured WO_3 photoanodes in a methanesulfonic acid (CH_3SO_3H) electrolyte [38], achieving large and stable photocurrent densities. They ascribed this good behavior to the minimization of the e^--h^+ recombination coming from the formation of a surface layer of tungsten peroxo-species, although the mechanism by which this was achieved in CH_3SO_3H solutions in particular was not clearly explained.

In order to investigate a way of suppressing or, at least, lessening the negative effects of the photo-induced generation of hydrogen peroxide on the stability of the WO_3 photoanodes, i_{ph}-U curves and stability tests were also performed in HCl, NaCl (pH adjusted to 0 by adding small amounts of highly concentrated (37%) HCl) and CH_3SO_3H electrolytes (**Figure 10**). In the case of the sample immersed in the methanesulfonic acid solution, it can be observed that recorded photocurrent densities were lower than those obtained in the electrolytes with Cl^-, regardless of the chloride concentration and the applied potential (**Figure 10a**). Moreover, it is evident from **Figure 10b** that WO_3 nanostructures were not stable in that solution under illumination (the photocurrent density decreased a 73% after 1h, a value similar to those reported above for 0.1M Na_2SO_4 and 0.1M H_2SO_4 electrolytes).

On the other hand, for the Cl⁻ containing electrolytes, it can be observed that photocurrent densities slightly decreased at 1.02 V as the chloride concentration increased (**Figure 10a**). This fact can be related to some interaction between the WO_3 nanostructure and the Cl⁻ anions, which led to a (minor) reduction in photoactivity. Regarding the stability of the photoanodes, WO_3 samples were more stable in concentrated chloride solutions (i.e 5M NaCl) than in diluted ones (**Figure 10b**), since the decrease experimented by photocurrent density in the 5M NaCl solution was the lowest (39%) (**Figure 10c**). This fact can be explained by taking into account two factors. As it has been explained above, Cl⁻ anions competed with H_2O for the valence band holes; thus, the oxidation of Cl⁻ to Cl_2 somewhat limited the incomplete water oxidation to hydrogen peroxide and hence moderately improved the photostability of the samples [56]. However, little differences can be discerned in the photocurrent density response of the samples immersed in the 1M HCl and 3M NaCl (pH 0), but this response was different in the 5M NaCl (pH 0) electrolyte, where the decrease in photocurrent density with time was not abrupt (**Figure 10b**). Therefore, the presence of Cl⁻ anions competing with water for the valence band holes was not the only factor that positively influenced the photoanode stability. The other factor was the reduction in the activity of water (a_W). In diluted or moderately concentrated electrolytes, a_W usually takes values very close to one; in highly concentrated solutions, however, a_W falls below unity, since hydration of ions removes water from the "role" of solvent to become a part of the hydrated ion, thus reducing its thermodynamic activity. Hence, a reduction in a_W with increasing electrolyte concentration can be understood as a reduction in the amount of free H_2O molecules in the solution. Since water was the reacting species in the

formation of hydrogen peroxide and hydroxyl radicals, according to eq. (16) and eq. (17), a reduction in a_W led to a reduction in the formation of H_2O_2 and •OH.

From osmotic coefficient values (ϕ) of NaCl solutions [61, 62], a_W has been calculated according to the next equation [63, 64]:

$$\ln(a_W) = -\phi M_W \varsigma m \qquad (18)$$

where M_W is the molar mass of water and ς is the stoichiometric parameter, i.e., the number of ion moles produced by complete dissociation of one mole of salt (for a 1:1 salt such as NaCl or LiCl, ς equals 2); notice that molality m is expressed in kilomole of solute per kilogram of solvent (or mole of solute per gram of solvent) so the units in eq. (18) are consistent. In the present case, a_W for the 3M NaCl electrolyte is 0.88, while a_W for the 5M NaCl electrolyte is 0.78. Consequently, this decrease in a_W contributed to stabilize to some extent the photoanode immersed in the latter electrolyte by reducing the formation of hydrogen peroxide and hydroxyl radicals through eq. (16) and eq. (17).

Since a decrease in a_W has been observed to positively affect the photoresponse of the WO_3 nanostructures in terms of an improvement of their photodegradation resistance, additional photoelectrochemical tests were carried out in highly concentrated chloride solutions. In NaCl electrolytes, a_W cannot be decreased below a value of ~0.75 [61], so LiCl solutions were used instead for that purpose. Given that the Li^+ cation is smaller than the Na^+ one but both have the same charge, the smallest cation produces the strongest electrical field, resulting in stronger interactions with the surrounding water molecules. Thus, working with LiCl solutions, a_W can be further reduced [65]. In

Figure 11, the variation of a_W with molar concentration for LiCl electrolytes is plotted. It can be observed that a_W continuously decreases as LiCl concentration increases, this effect being more marked at high concentrations, where a_W values are very low, close to zero. In this figure, activity of Cl$^-$ anions is also represented against the molar concentration of LiCl. This activity, a_{LiCl}, has been calculated from the following equation:

$$a_{LiCl} = \frac{m_{LiCl}}{m^0}\gamma_\pm \tag{19}$$

where the LiCl molality, m_{LiCl}, is defined as mol LiCl/kg H$_2$O and m^0 is the standard LiCl molality (m^0 = 1 mol LiCl/kg H$_2$O). Activity coefficients and osmotic coefficients have been obtained from the literature [61], as well as density values of LiCl aqueous electrolytes used to transform molality to molarity [66].

Figure 12a shows the i_{ph}-U curves of the sample anodized at 500 rpm and immersed in several concentrated LiCl electrolytes. It can be observed that i_{ph} values decreased to some extent as the LiCl concentration increased, as it was also observed in **Figure 10a**. This fact may be explained by some negative interaction between chlorides and WO$_3$, taking into account that activity of Cl$^-$ anions sharply increased for LiCl concentrations higher than 5M (**Figure 11**). On the other hand, in spite of the lower photocurrent density values, it is evident that WO$_3$ nanostructures became more stable as LiCl concentration increased (**Figure 12b** and **Figure 12c**), due to the reduction of a_w, as explained above: in the 5M LiCl electrolyte, a_w = 0.7, while in the 13.3M LiCl solution a_w = 0.1, so the generation of H$_2$O$_2$ and hydroxyl radicals via eq. (16) and eq. (17),

respectively, was significantly reduced in the most concentrated LiCl electrolyte, this reduction positively affecting the stability of the samples.

Nonetheless, and despite the better performance of WO_3 nanostructures in low a_W electrolytes in terms of its photodegradation resistance, photocurrent density values obtained from the i_{ph}-U curves were appreciably lower in highly concentrated Cl⁻ solutions than, for example, in 0.1M H_2SO_4. In consequence, the next step was to keep the values of a_W low, thus ensuring the good stability of the samples, but to increase at the same time photocurrent densities. The ability of alcohols to reduce the activity of water is well known [67, 68]. On the other hand, a high ionic conductivity within the WO_3 nanostructures is crucial to prevent uneven current and potential distributions across the nanostructured semiconductor electrode [38], which would negatively affect its photoelectrochemical performance. Methanol possesses an electrical conductivity higher than other alcohols [69] and, as it has been observed above (**Figure 9**), the role of methanol as a hole scavenger resulted in a considerable increase in photocurrent density due to the direct injection of an electron to the WO_3 conduction band (eq. (14)). In that sense, a_W has been reduced by adding different amounts of CH_3OH to a 5M LiCl aqueous electrolyte: 4 mol% CH_3OH (1M; $a_W \approx 0.7$), 36 mol% CH_3OH ($a_W \approx 0.5$), 65 mol% CH_3OH ($a_W \approx 0.3$), water-free CH_3OH solution ($a_W \approx 0$). Activity of water values in these solutions have been estimated from the literature [67, 68], taking the values of a_W shown in **Figure 11** for aqueous LiCl solutions as starting point. In the i_{ph}-U curves for the different CH_3OH-LiCl electrolytes (**Figure 13a)** it can be observed that photocurrent densities increased as the mol% of CH_3OH increased, except for the water-free CH_3OH solution, in which i_{ph} took the lowest values of the series. Moreover, photocurrent densities were considerably higher than those obtained in LiCl aqueous

solutions (**Figure 12a**), which can be explained by the additional electron injected in the WO$_3$ valence band during the oxidation of the adsorbed intermediate radical, •CH$_2$OH(ads) (eq. (14)). In the water-free CH$_3$OH solution, the decrease observed in i_{ph} was most likely due to a decrease in the ionic conductivity of the solution (the conductivity of water-free 5M LiCl/methanol is 11.89 mS cm^{-1}, while that of 5M LiCl/65 mol% methanol/water is 22.6 mS cm^{-1}).

Concerning the stability of the WO$_3$ nanostructures immersed in these electrolytes, an increase in the mol% of CH$_3$OH increased the resistance of the samples to photodegradation, since the decrease (in %) of i_{ph} in 1h was manifestly reduced to a value below 10% in the 65 mol% CH$_3$OH solution; in the water-free CH$_3$OH solution i_{ph} even increased in 5.3%, although photocurrent densities were lower than in the 65 mol% CH$_3$OH solution. These results confirm the beneficial influence that a reduction in a_W had on the resistance of the WO$_3$ nanostructures to undergo H$_2$O$_2$-driven photodegradation. Moreover, the reduction in a_W achieved by adding CH$_3$OH to the 5M LiCl solution avoided the negative effect that elevated chloride activities had on the photoelectrochemical performance of the samples, without leading to an excessive decrease in ionic conductivity, due to the high concentration of LiCl.

3.5. Photoelectrochemical activity

Photocatalytic H$_2$ production from methanol-containing solutions has previously been reported in the literature [54, 70-73]. In these cases, H$_2$ was the main gaseous product evolving on the cathode, while CO$_2$ evolved on the anode after more or less prolonged irradiation due to the complete oxidation of CH$_3$OH [54, 71]. The direct oxidation of

methanol by surface holes starts with eq. (13) and eq. (14) and continues as follows [54]:

$$CH_2O\,(ads) + h^+ \rightarrow CHO\cdot(ads) + H^+ \qquad \textbf{(20)}$$

$$CHO\cdot(ads) + h^+ + H_2O \rightarrow CHOOH\,(ads) + H^+ \qquad \textbf{(21)}$$

$$CHOOH\,(ads) + h^+ \rightarrow CHOO\cdot(ads) + H^+ \qquad \textbf{(22)}$$

$$CHOO\cdot(ads) + h^+ \rightarrow CO_2\,(ads) + H^+ \qquad \textbf{(23)}$$
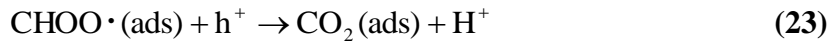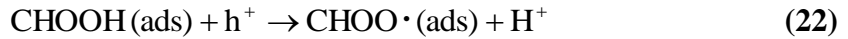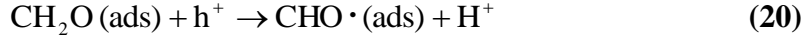
The complete oxidation of methanol via eqs. (13), (14), (20)-(23) involves the formation of $6H^+$ per mol of CH_3OH, so the cathodic reaction is:

$$6H^+ + 6e^- \rightarrow 3H_2\,(g) \qquad \textbf{(24)}$$

And the overall reaction is:

$$CH_3OH + H_2O \rightarrow CO_2\,(g) + 3H_2\,(g) \qquad \textbf{(25)}$$

These overall methanol decomposition has a lower splitting energy than water (0.7 eV vs. 1.23 eV) [72]. In a recent work by Lin et. al [72], it was observed that the maximum hydrogen production using a $Pt/TiO_{2-x}N_x$ catalyst was achieved in a solution 80 vol% of methanol, which corresponds approximately to a 65 mol% CH_3OH. Hence, in concentrated methanolic aqueous solutions, the photogeneration of H_2 seems to be enhanced, while CO_2 evolves on the anode. In the present case, where the methanol/water solution also has 5M LiCl, gaseous Cl_2, as well as some O_2, may also form on the anode.

Figure 14 shows the i_{ph}-U curves and the photocurrent density transients recorded for 1 hour under simulated sunlight of the different WO_3 samples anodized at various rotation velocities, immersed in the 5M LiCl with 65 mol% CH_3OH electrolyte. It can be observed that the relationship between photocurrent density values and rotation velocity is not direct. The sample anodized at 375 rpm provided the highest photoresponse, which is consistent with this sample having the largest electrochemically active surface area. This sample was followed by those synthesized at 250, 500 and 750 rpm (in that order), which also presented high photocurrent densities, while the photoresponse of the samples anodized at 125 and 1000 rpm was significantly lower. Finally, the WO_3 nanoplatelets formed under static flow conditions (0 rpm) provided the lowest photocurrent density. These results are consistent with the previous findings, since samples synthesized at low (0 and 125 rpm) and high (1000 rpm) rotation velocities presented lower electrochemically active surface areas and higher charge-transfer resistance values than those anodized at intermediate rpm (250-500 rpm).

Figure 15 shows the $(i_{ph}\ hv)^{0.5}$ vs. hv plots for the different samples obtained by measuring the photocurrent density of the WO_3 nanoplatelets at an applied potencial of 1.02 $V_{Ag/AgCl}$ in the wavelength range from 300 to 500 nm. These plots have been used to determine the indirect band-gap energy (E_g) of the nanostructures, where h is Planck's constant (4.1357×10^{-15} eV·s) and v is the frequency of light. The E_g values, obtained from the x-intercept of the extrapolated linear part of the diagram, are shown in **Table 2**. The calculated E_g are slightly lower than the typical value for crystalline WO_3 (2.6 eV) [6]. This slight red shift can be explained by an enhancement in light scattering due to the nanoplatelet morphology resulting in higher light adsorption by the

nanostructures [30]. No appreciable differences in E_g were observed for samples anodized at different rotation velocities.

CONCLUSIONS

Globular clusters of WO_3 nanoplatelets associated in a tree-like fashion have been obtained by anodizing W in an acidic F-containing electrolyte under controlled hydrodynamic conditions. The thickest nanoplatelets layers were obtained at 375 rpm, since this rotation velocity was high enough to enhance mass transfer towards the electrode surface and hence to increase the formation of soluble species and their subsequent precipitation in the form of hydrated WO_3, but it was not too high as to facilitate the removal of these soluble species from the electrode surrounding area.

The charge-transfer resistance at the nanostructure/electrolyte interface decreased for the samples anodized at intermediate rotation velocities (250-500 rpm), while the double layer capacitance increased for these samples, which can be explained by an increase of their electrochemically active surface area.

Mott-Schottky analysis concluded that tree-like WO_3 nanoplatelets synthesized at intermediate rotation velocities (250-500 rpm) had the highest concentration of oxygen vacancies in their crystalline structures, resulting in higher electrical conductivities, which is consistent with the decrease in the charge-transfer resistance observed through EIS measurements.

WO$_3$ nanostructures were not stable in alkaline media due to the active dissolution of the oxide by the action of OH$^-$. Moreover, these nanostructures were not resistant to photodegradation in aqueous acidic electrolytes with low ionic strengths due to the photogeneration of peroxides and hydroxyl radicals that interacted with the surface of the electrode and resulted in a gradual loss of photoactivity. In highly concentrated chloride solutions the stability of the samples manifestly improved due to the reduction of the activity of water, which led to a decrease in the formation of peroxides and hydroxyl radicals. However, the photoactivity of the samples decreased with increasing chloride activity, so aqueous/methanolic mixed solutions with high chloride concentration were used in the end to assure a very good photostability of the samples.

Apart from being a hole scavenger and helping in the separation of photogenerated electron-hole pairs, methanol has been demonstrated to play an important role in reducing the activity of water and thus the H$_2$O$_2$-induced photodegradation of WO$_3$ nanoplatelets. The suppression of peroxide species remarkably improved the long-term photostability of WO$_3$.

Photocurrent densities measured indicated the superior photocatalytic activity of tree-like WO$_3$ nanoplatelets synthesized at intermediate rotation velocities, especially at 375 rpm, which was attributed to their higher efficiency for electron transfer due to their larger surface area. These results indicate that photoelectrochemical efficiency of WO$_3$ nanoplatelets can be largely enhanced simply by anodizing W under controlled hydrodynamic conditions at a rotation velocity of 375 rpm.

REFERENCES

[1]   H. E. Prakasam, K. Shankar, M. Paulose, O. K. Varghese, C. A. Grimes, J. Phys. Chem. C 111 (2007) 7235-7241.

[2]   P. Roy, S. Berger, P. Schmuki, Angew. Chem. Int. Ed. 50 (2011) 2904-2939.

[3]   R. Sánchez-Tovar, R. M. Fernández-Domene, D. M. García-García, J. García-Antón, J. Power Sources 286 (2015) 224-231.

[4]   H. Tsuchiya, J. M. Macak, I. Sieber, L. Taveira, A. Ghicov, K. Sirotna, P. Schmuki, Electrochem. Commun. 7 (2005) 295-298.

[5]   E. Widenkvist, R. A. Quinlan, B. C. Holloway, H. Grennberg, U. Jansson, Cryst. Growth Des. 8 (2008) 3750-3753.

[6]   H. Zheng, J. Z. Ou, M. S. Strano, R. B. Kaner, A. Mitchell, K. Kalantar-zadeh. Nanostructured Tungsten Oxide - Properties, Synthesis, and Applications, Adv. Funct. Mater. 21 (2011) 2175-2196.

[7]   V. Chakrapani, J. Thangala, M. K. Sunkara, Int. J. Hydrogen Energ. 34 (2009) 9050-9059.

[8]   V. Cristino, S. Caramori, R. Argazzi, L. Meda, G. L. Marra, C. A. Bignozzi, Langmuir 27 (2011) 7276-7284.

[9]   F. Amano, M. Tian, B. Ohtani, A. Chen, J. Solid State Electrochem. 16 (2012) 1965-1973.

[10] Q. Chen, J. Li, B. Zhou, M. Long, H. Chen, Y. Liu, W. Cai, W. Shangguan, Electrochem. Commun. 20 (2012) 153-156.

[11] S. M. Ahmed, J. Leduc, S. F. Haller, J. Phys. Chem. 92 (1988) 6655-6660.

[12] K. Sivula, F. Le Formal, M. Grätzel, ChemSusChem 4 (2011) 432-449.

[13] S. J. Kim, J. Choi, Electrochem. Commun. 10 (2008) 175-179.

[14] J. Zhao, X. Wang, J. Liu, Y. Meng, X. Xu, C. Tang, Mater. Chem. Phys. 126 (2011) 555-559.

[15] T. Bak, J. Nowotny, M. Rekas, C. C. Sorrell, Int. J. Hydrogen Energ. 27 (2002) 991-1022.

[16] S. Chen, L.-W. Wang, Chem. Mater. 24 (2012) 3659-3666.

[17] A. Watcharenwong, W. Chanmanee, N. R. de Tacconi, C. R. Chenthamarakshan, P. Kajitvichyanukul, K. Rajeshwar, J. Electroanal. Chem. 612 (2008) 112-120.

[18] A. Z. Sadek, H. Zheng, M. Breedon, V. Bansal, S. K. Bhargava, K. Latham, J. Zhu, L. Yu, Z. Hu, P. G. Spizzirri, W. Wlodarski, K. Kalantar-zadeh, Langmuir 25 (2009) 9545-9551.

[19] H. Zheng, A. Z. Sadek, K. Latham, K. Kalantar-zadeh, Electrochem. Commun. 11 (2009) 768-771.

[20] K. Kalantar-zadeh, A. Z. Sadek, H. Zheng, V. Bansal, S. K. Bhargava, W. Wlodarski, J. Zhu, L. Yu, Z. Hu, Sensor. Actuat. B-Chem. 142 (2009) 230-235.

[21] W. Lee, D. Kim, K. Lee, P. Roy, P. Schmuki, Electrochim. Acta 56 (2010) 828-833.

[22] Y. Liu, Y. Li, W. Li, S. Han, C. Liu, Appl. Surf. Sci. 258 (2012) 5038-5045.

[23] C. W. Lai, S. Sreekantan, Mat. Sci. Semicon. Proc. 16 (2013) 303-310.

[24] C. K. Wang, C. K. Lin, C. L. Wu, S. C. Wang, J. L. Huang, Electrochim. Acta 112 (2013) 24-31.

[25] C. Ng, Y. H. Ng, A. Iwase, R. Amal, ACS Appl. Mater. Inter. 5 (2013) 5269-5275.

[26] K. R. Reyes-Gil, C. Wiggenhorn, B. S. Brunschwig, N. S. Lewis, J. Phys. Chem. C 117 (2013) 14947-14957.

[27] W. Li, P. Da, Y. Zhang, Y. Wang, X. Lin, X. Gong, G. Zheng, ACS Nano 8 (2014) 11770-11777.

[28] J. H. Ha, P. Muralidharan, D. K. Kim, J. Alloy. Compd. 475 (2009) 446-451.

[29] C. Ng, C. Ye, Y. H. Ng, R. Amal, Cryst. Growth Des. 10 (2010) 3794-3801.

[30] J. Yang, W. Li, J. Li, D. Sun, Q. Chen, J. Mater. Chem. 22 (2012) 17744-17752.

[31] S. S. Kalanur, Y. J. Hwang, S. Y. Chae, O. S. Joo, J. Mater. Chem. A 1 (2013) 3479-3488.

[32] M. Anik, T. Cansizoglu, J. Appl. Electrochem. 36 (2006) 603-608.

[33] C. A. Bignozzi, S. Caramori, V. Cristino, R. Argazzi, L. Meda, A. Tacca, Chem. Soc. Rev. 42 (2013) 2228-2246.

[34] J. M. Spurgeon, J. M. Velazquez, M. T. McDowell, Phys. Chem. Chem. Phys. 16 (2014) 3623-3631.

[35] W. Li, J. Li, X. Wang, J. Ma, Q. Chen, Int. J. Hydrogen Energ. 35 (2010) 13137-13145.

[36] M. Yagi, S. Maruyama, K. Sone, K. Nagai, T. Norimatsu, J. Solid State Chem. 181 (2008) 175-182.

[37] J. A. Seabold, K. S. Choi, Chem. Mater. 23 (2011) 1105-1112.

[38] R. Solarska, R. Jurczakowski, J. Augustynski, Nanoscale 4 (2012) 1553-1556.

[39] R. M. Fernández-Domene, R. Sánchez-Tovar, E. Segura-Sanchís, J. García-Antón, Chem. Eng. J. 286 (2016) 59-67.

[40] J. Z. Ou, M. Z. Ahmad, K. Latham, K. Kalantar-zadeh, G. Sberveglieri, W. Wlodarski, Procedia Engineering 25 (2011) 247-251.

[41] W. Li, J. Li, X. Wang, S. Luo, J. Xiao, Q. Chen, Electrochim. Acta 56 (2010) 620-625.

[42] A. Di Paola, F. Di Quarto, C. Sunseri, Corros. Sci. 20 (1980) 1067-1078.

[43] A. J. Bard and L. R. Faulkner, Electrochemical Methods: Fundamentals and Applications, John Wiley & Sons, New York, NY, 2001.

[44] G. J. Brug, A. L. G. van den Eeden, M. Sluyters-Rehbach, J. H. Sluyters, J. Electroanal. Chem. 176 (1984) 275-295.

[45] B. Hirschorn, M. E. Orazem, B. Tribollet, V. Vivier, I. Frateur, M. Musiani, Electrochim. Acta 55 (2010) 6218-6227.

[46] J. O. Bockris, J. Appl. Phys. 52 (1981) 808-810.

[47] K. Uosaki, H. Kita, J. Electrochem. Soc. 130 (1983) 895-897.

[48] R. M. Fernández-Domene, E. Blasco-Tamarit, D. M. García-García, J. García-Antón, Electrochim. Acta 95 (2013) 1-11.

[49] G. Wang, Y. Ling, H. Wang, X. Yang, C. Wang, J. Z. Zhang, Y. Li, Energy Environ. Sci. 5 (2012) 6180-6187.

[50] C. R. Lhermitte, J. G. Verwer, B. M. Bartlett, J. Mater. Chem. A DOI: 10.1039/C5TA04747A (2016) .

[51] R. van de Krol, Principles of Photoelectrochemical Cells, in: R. van de Krol, M. Grätzel (eds.), Photoelectrochemical Hydrogen Production, New York, 2012.

[52] A. Hagfeldt, H. Lindström, S. Södergren, S. E. Lindquist, J. Electroanal. Chem. 381 (1995) 39-46.

[53] C. Santato, M. Ulmann, J. Augustynski, J. Phys. Chem. B 105 (2001) 936-940.

[54] J. Chen, D. F. Ollis, W. H. Rulkens, H. Bruning, Wat. Res. 33 (1999) 669-676.

[55] M. Ulmann, N. R. de Tacconi, J. Augustynski, J. Phys. Chem. 90 (1986) 6523-6530.

[56] J. C. Hill, K. S. Choi, J. Phys. Chem. C 116 (2012) 7612-7620.

[57] Q. Mi, A. Zhanaidarova, B. S. Brunschwig, H. B. Gray, N. S. Lewis, Energy Environ. Sci. 5 (2012) 5694-5700.

[58] J. Zhao, E. Olide, F. E. Osterloh, J. Electrochem. Soc. 162 (2015) H65-H71.

[59] L. Weinhardt, M. Blum, M. Bär, C. Heske, B. Cole, B. Marsen, E. L. Miller, J. Phys. Chem. C 112 (2008) 3078-3082.

[60] Q. Mi, R. H. Coridan, B. S. Brunschwig, H. B. Gray, N. S. Lewis, Energy Environ. Sci. 6 (2013) 2646-2653.

[61] W. J. Hamer, Y.-C. Wu, J. Phys. Chem. Ref. Data 1 (1972) 1047-1075.

[62] K. S. Pitzer, J. C. Peiper, R. H. Busey, J. Phys. Chem. Ref. Data 13 (1984) 1-102.

[63] J. M. Prausnitz, R. N. Lichtenthaler, and E. G. Azevedo, Molecular Thermodynamics of Fluid-Phase Equilibria, Prentice Hall, Upper Saddle River, NJ, 1999.

[64] M. J. Blandamer, J. B. F. N. Engberts, P. T. Gleeson, J. C. R. Reis, Chem. Soc. Rev. 34 (2005) 440-458.

[65] C. Held, L. F. Cameretti, G. Sadowski, Fluid Phase Equilibria 270 (2008) 87-96.

[66] I. M. Abdulagatov, N. D. Azizov, Chem. Geol. 230 (2006) 22-41.

[67] P. S. Crozier, R. L. Rowley, Fluid Phase Equilibr. 193 (2002) 53-73.

[68] G. C. Nihous, C. K. Kinoshita, S. M. Masutani, Chem. Eng. Sci. 64 (2009) 2767-2771.

[69] M. Prego, O. Cabeza, E. Carballo, C. F. Franjo, E. Jiménez, J. Mol. Liq. 89 (2000) 233-238.

[70] J. Chen, D. F. Ollis, W. H. Rulkens, H. Bruning, Wat. Res. 33 (1999) 661-668.

[71] T. Kawai, T. Sakata, J. Chem. Soc. Chem. Comm. (1980) 694-695.

[72] W. C. Lin, W. D. Yang, I. L. Huang, T. S. Wu, Z. J. Chung, Energ. Fuel 23 (2009) 2192-2196.

[73] A. Galinska, J. Walendziewski, Energ. Fuel 19 (2005) 1143-1147.

Tables captions

Table 1. Donor density (N_D) and flat-band potential (U_{FB}) of the WO$_3$ nanoplatelets formed at different rotation velocities.

Table 2. Band-gap values of the WO$_3$ nanoplatelets formed at different rotation velocities.

Figures captions

Figure 1. FE-SEM images of the WO$_3$ nanostructures formed upon anodization of W in a 1.5M H$_2$SO$_4$ + 0.1M NaF electrolyte at 50º C, imposing a potential of 20V for 4 hours, under different hydrodynamic conditions: (a) 0 rpm, (b) 125 rpm, (c) 250 rpm, (d) 375 rpm, (e) 500 rpm, (f) 750 rpm, and (g) 1000 rpm.

Figure 2. Nanoplatelets layer thickness and % of covered surface as a function of the rotation velocity (a). FE-SEM cross-sectional images of samples anodized at 0 rpm (left) and 500 rpm (right).

Figure 3. Current density transient recorded during anodization for all the samples.

Figure 4. Experimental Nyquist (a) and Bode-phase (b) diagrams for the WO$_3$ nanoplatelets formed at different rotation velocities.

Figure 5. Electrical equivalent circuits used to simulate the experimental EIS data for the WO$_3$ nanoplatelets formed at (a) 0, 125, 250 and 375 rpm; (b) 500, 750 and 1000 rpm.

Figure 6. Values of the charge-transfer resistance (R_{nano}) and the double layer capacitance (C_{nano}) of the WO$_3$ nanoplatelets formed at different rotation velocities.

Figure 7. Mott-Schottky plots for the WO_3 nanoplatelets formed at different rotation velocities.

Figure 8. (a) Photocurrent density (i_{ph}) vs. potential (U) curves of the WO_3 nanostructure formed at 500 rpm measured in 0.1M Na_2SO_4, 0.1M H_2SO_4 and 0.1M KOH solutions under AM1.5 illumination. (b) Photocurrent density transients under illumination obtained at an applied potential of 1.02 $V_{Ag/AgCl}$ in the 0.1M Na_2SO_4 and 0.1M H_2SO_4 electrolytes.

Figure 9. (a) Photocurrent density (i_{ph}) vs. potential (U) curves of the WO_3 nanostructure formed at 500 rpm measured in 0.1M H_2SO_4 and 0.1M H_2SO_4 + 1M CH_3OH solutions under AM1.5 illumination. (b) Photocurrent density transients under illumination obtained at an applied potential of 1.02 $V_{Ag/AgCl}$ in the same electrolytes.

Figure 10. (a) Photocurrent density (i_{ph}) vs. potential (U) curves of the WO_3 nanostructure formed at 500 rpm measured in 0.1M HCl, 1M HCl, 3M NaCl, 5M NaCl and 1M CH_3SO_3H solutions under AM1.5 illumination. (b) Photocurrent density transients under illumination obtained at an applied potential of 1.02 $V_{Ag/AgCl}$ in the same electrolytes. (c) Values of photocurrent density before and after the stability tests and % of photocurrent density decrease in the same electrolytes as before.

Figure 11. Variation of activity of chloride ions (a_{LiCl}) and activity of water (a_W) with the LiCl molar concentration.

Figure 12. (a) Photocurrent density (i_{ph}) vs. potential (U) curves of the WO_3 nanostructure formed at 500 rpm measured in 5M LiCl, 7.2M LiCl, 9.6M LiCl and 13.3M LiCl solutions under AM1.5 illumination. (b) Photocurrent density transients under illumination obtained at an applied potential of 1.02 $V_{Ag/AgCl}$ in the same electrolytes. (c) Values of photocurrent density before and after the stability tests and % of photocurrent density decrease in the same electrolytes as before.

Figure 13. (a) Photocurrent density (i_{ph}) vs. potential (U) curves of the WO_3 nanostructure formed at 500 rpm measured in different aqueous/methanolic solutions with 5M LiCl under AM1.5 illumination. (b) Photocurrent density transients under illumination obtained at an applied potential of 1.02 $V_{Ag/AgCl}$ in the same electrolytes. (c) Values of photocurrent density before and after the stability tests and % of photocurrent density decrease in the same electrolytes as before.

Figure 14. (a) Photocurrent density (i_{ph}) vs. potential (U) curves of the WO_3 nanoplatelets formed at different rotation velocities, measured in a 65 mol% CH_3OH with 5M LiCl solution under AM1.5 illumination. (b) Photocurrent density transients under illumination obtained at an applied potential of 1.02 $V_{Ag/AgCl}$ in the same electrolyte.

Figure 15. Band-gap determination for the WO_3 nanoplatelets formed at different rotation velocities from the $(i_{ph} h\nu)^{0.5}$ vs. $h\nu$ plots.

Table 1

Sample (rpm)	N_D ($\times 10^{22}$ cm^{-3})	U_{FB}/V$_{Ag/AgCl}$
0	1.2 ± 0.3	0.30 ± 0.07
125	2.4 ± 0.2	0.29 ± 0.03
250	49.5 ± 19.1	0.28 ± 0.06
375	41.9 ± 8.1	0.32 ± 0.07
500	57.3 ± 13.5	0.23 ± 0.01
750	14.3 ± 0.5	0.30 ± 0.01
1000	10.5 ± 0.1	0.23 ± 0.02

Table 2

Sample (rpm)	E_g/eV
0	2.55 ± 0.04
125	2.53 ± 0.03
250	2.49 ± 0.02
375	2.48 ± 0.03
500	2.49 ± 0.04
750	2.53 ± 0.05
1000	2.52 ± 0.06

Figure 1
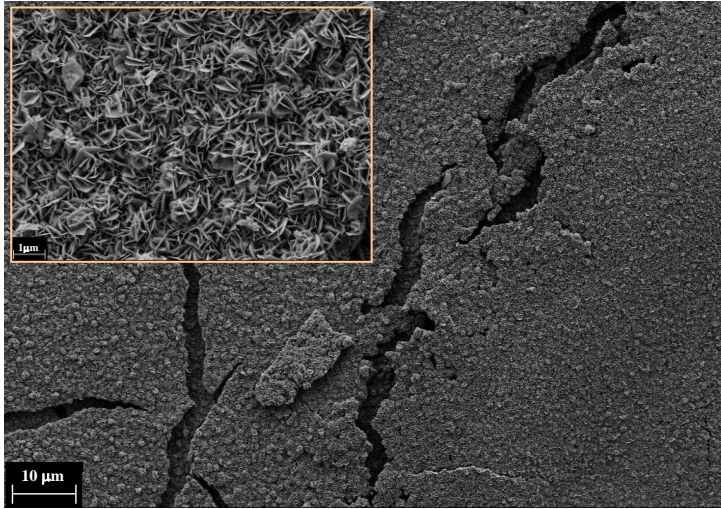
(a)
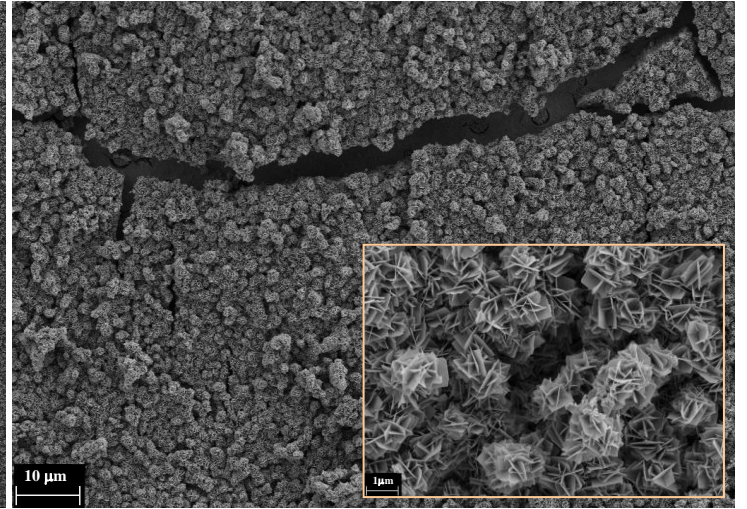
(b)
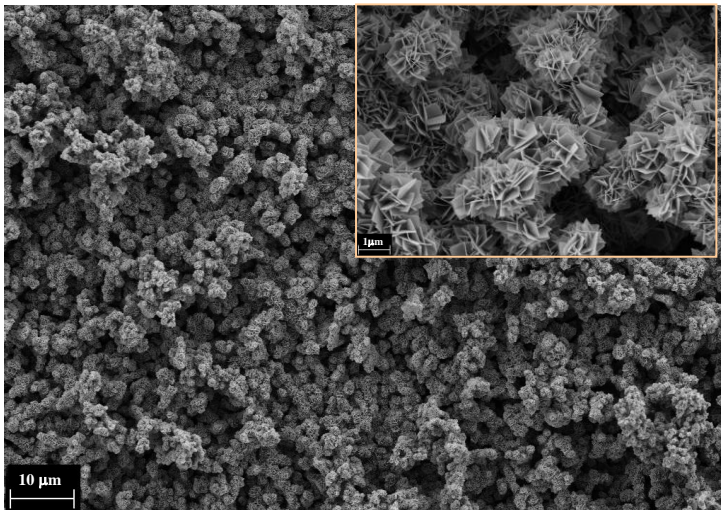
(c)
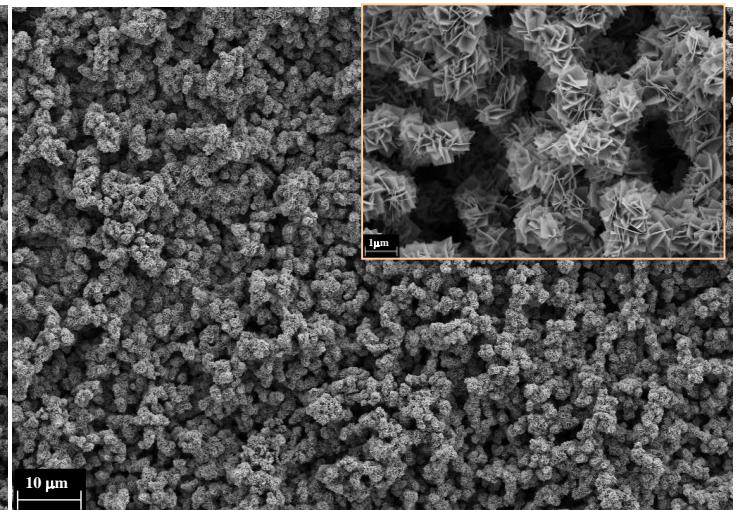
(d)
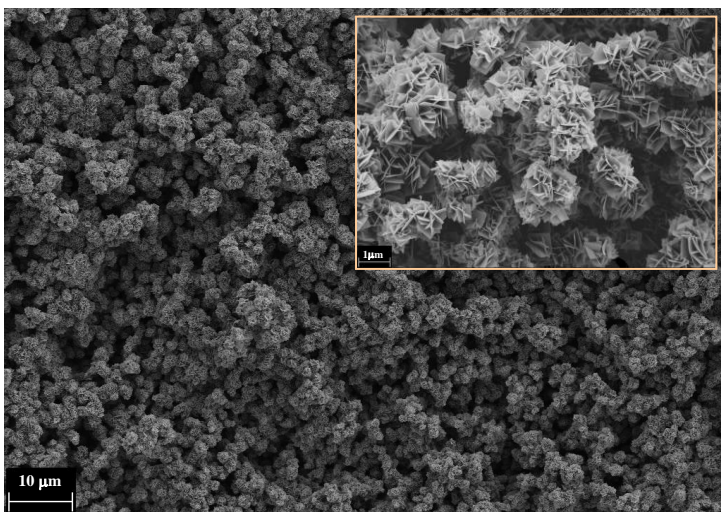
(e)
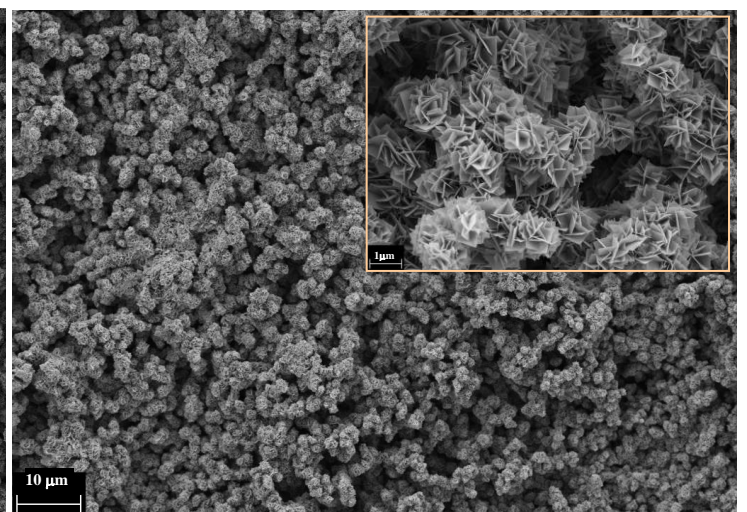
(f)
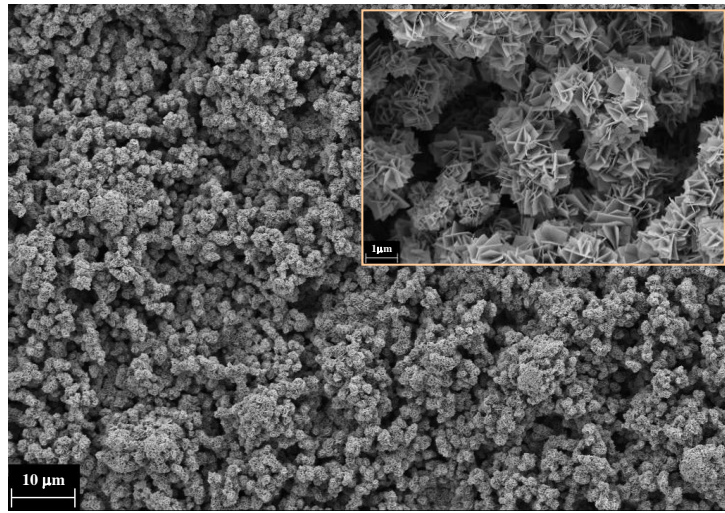
(g)

Figure 2
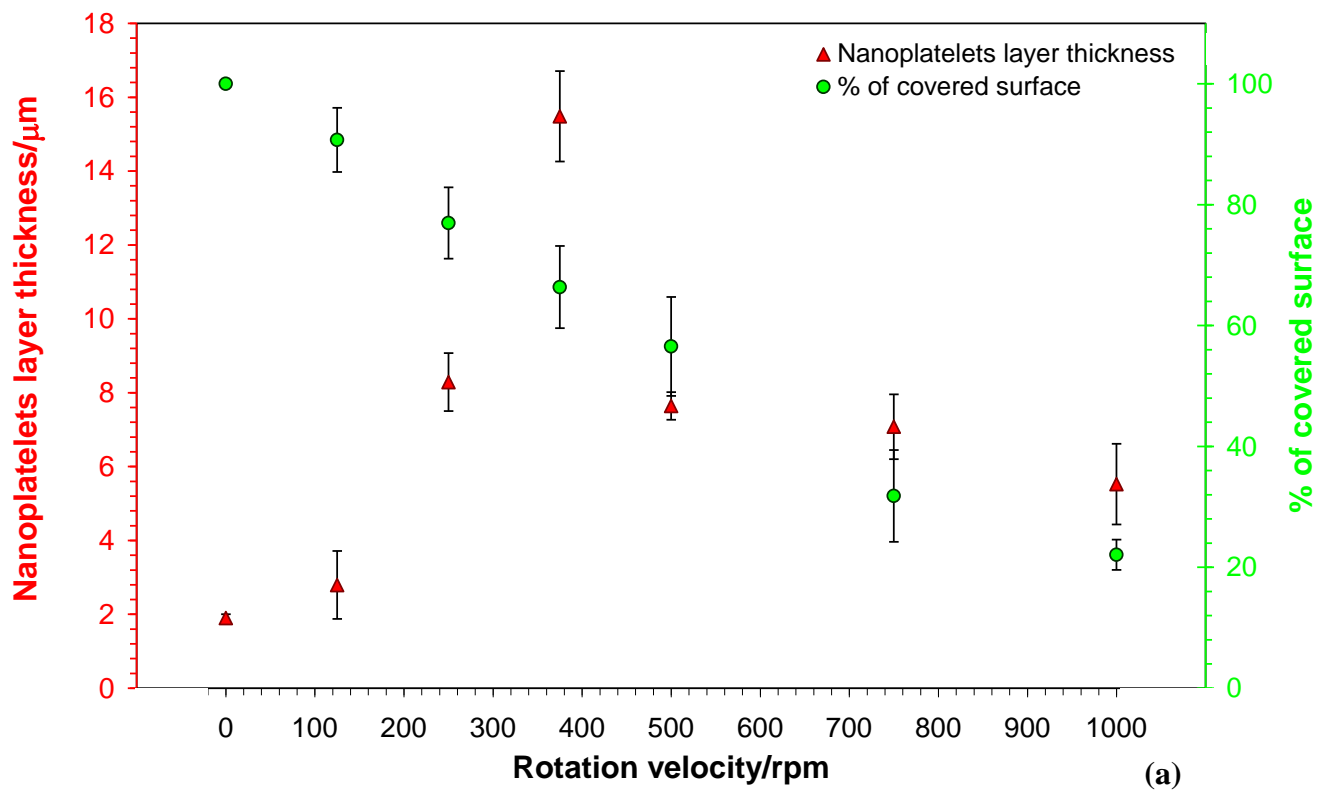
(a)

(b)

Figure 3

Figure 4

(a)

(b)
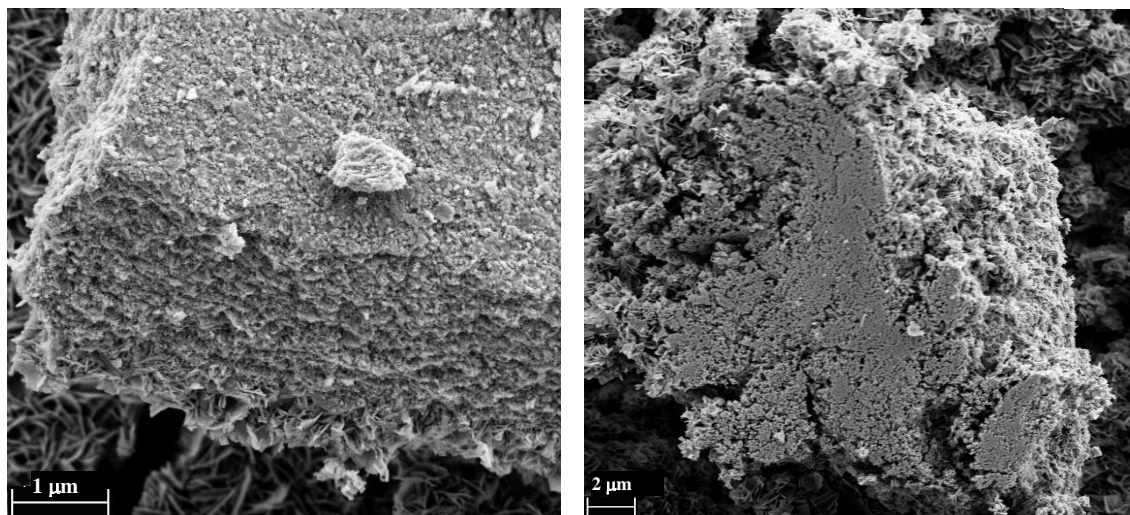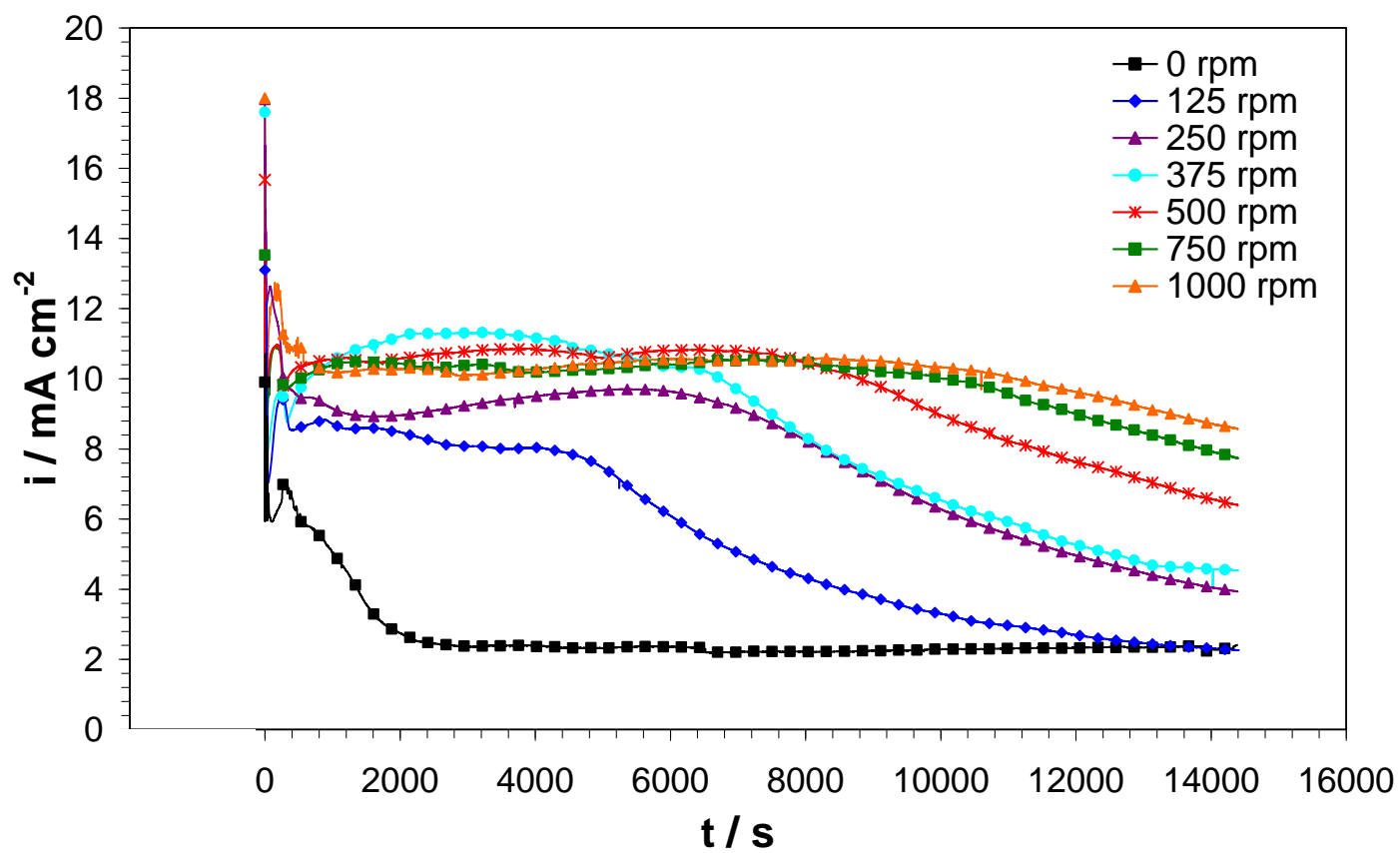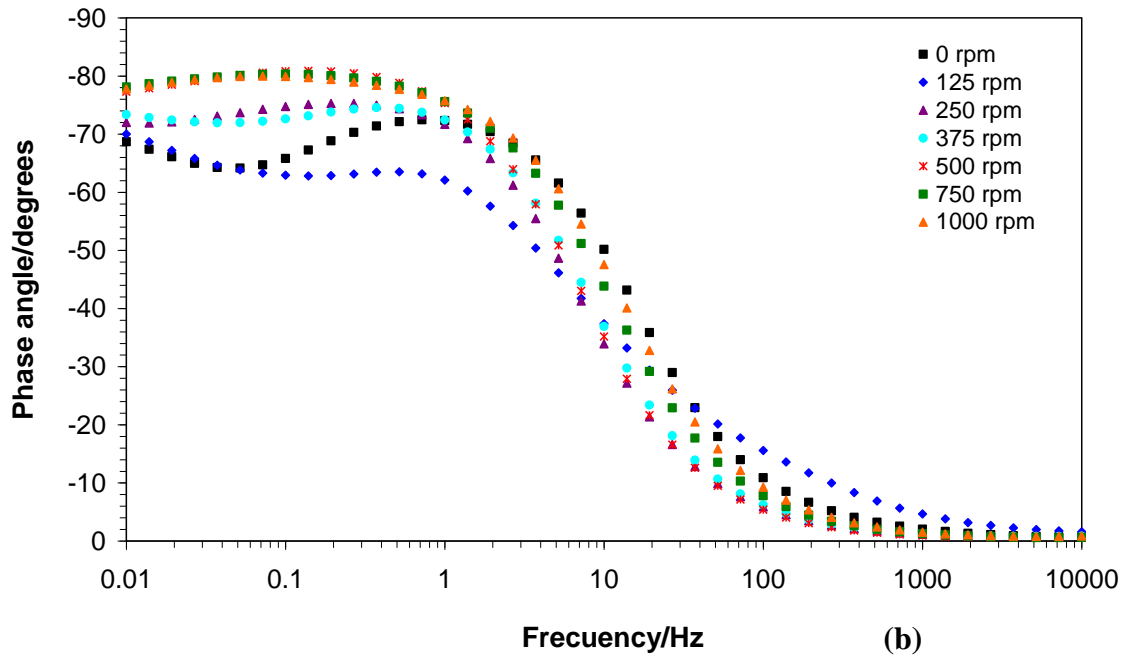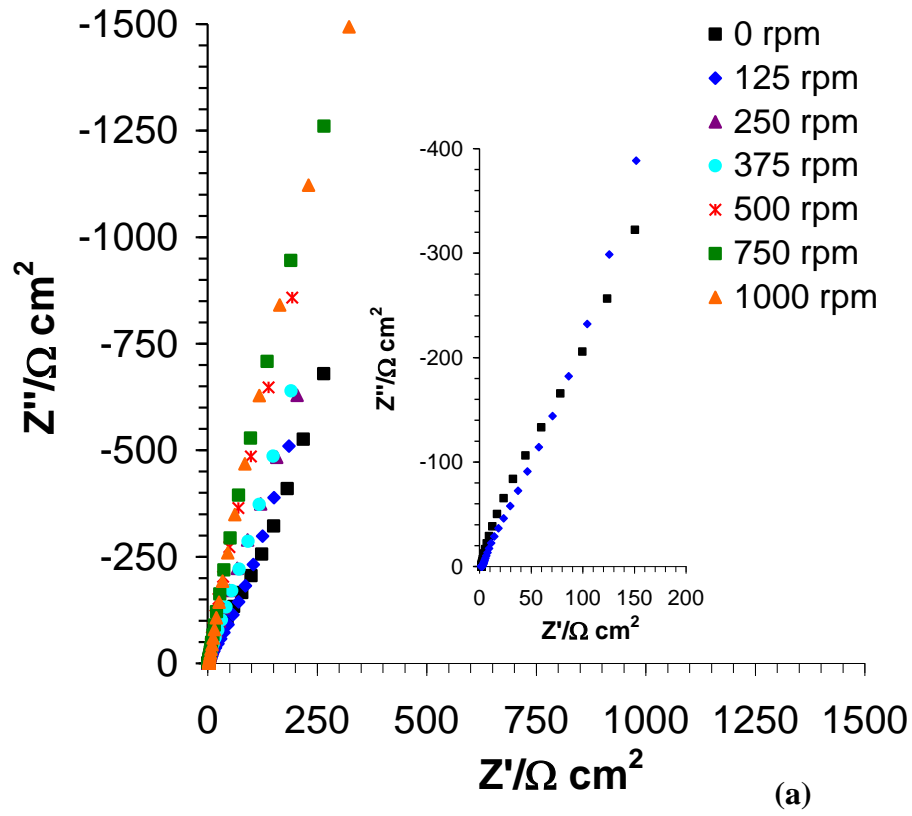
Figure 5

(a)

(b)

Figure 6

Figure 7

Figure 8

(a)

(b)

Figure 9

Figure 10

(a)

(b)

(c)
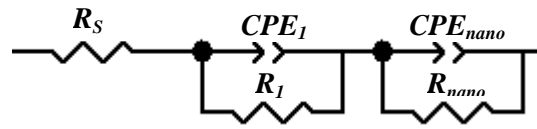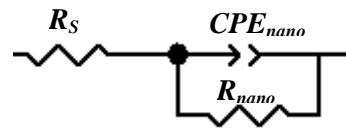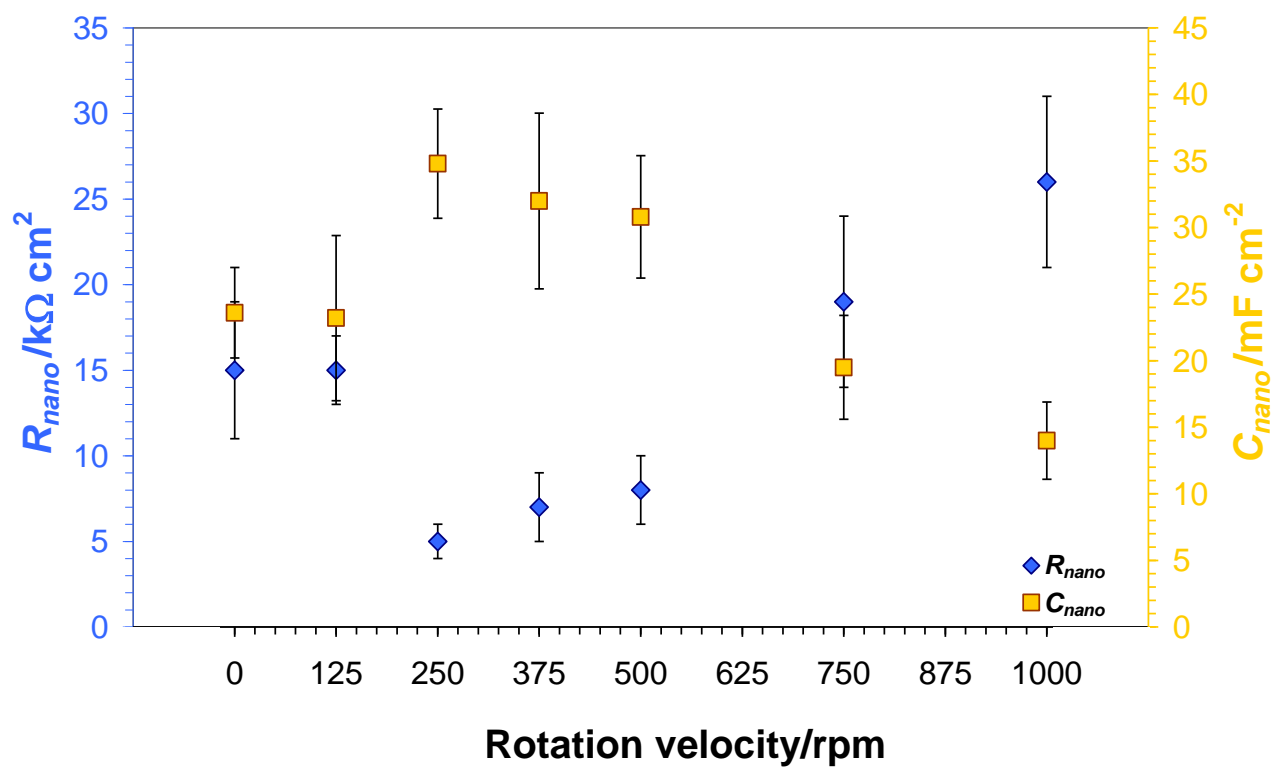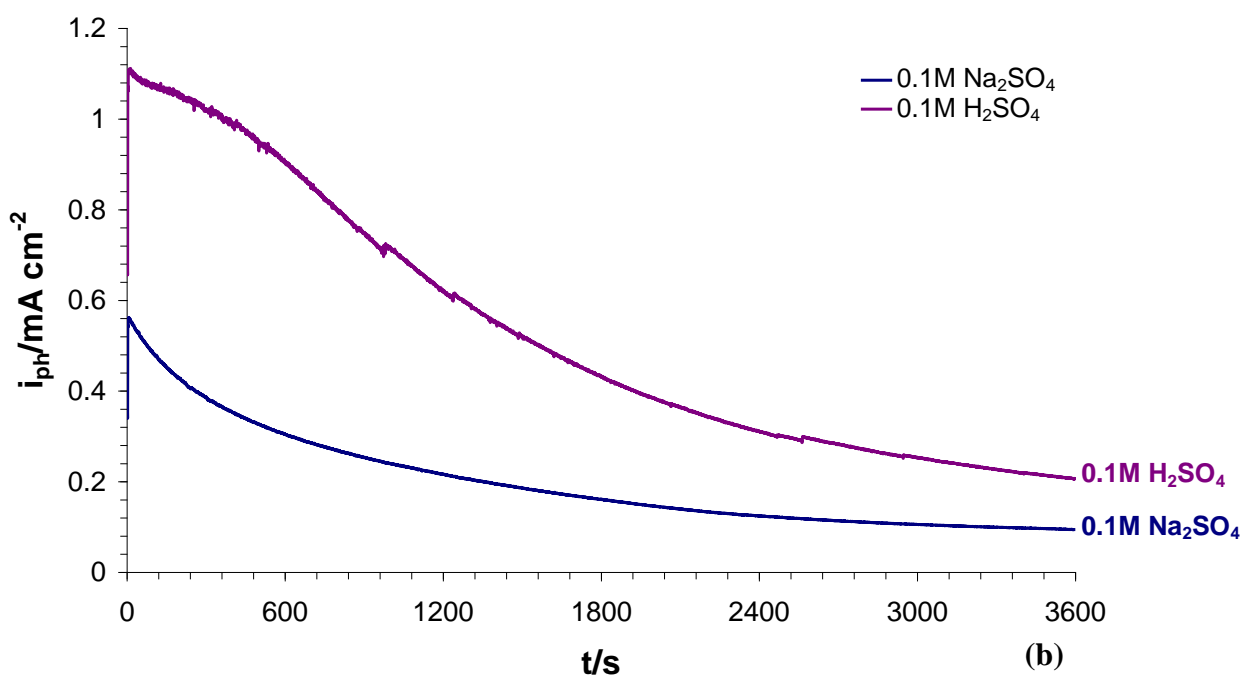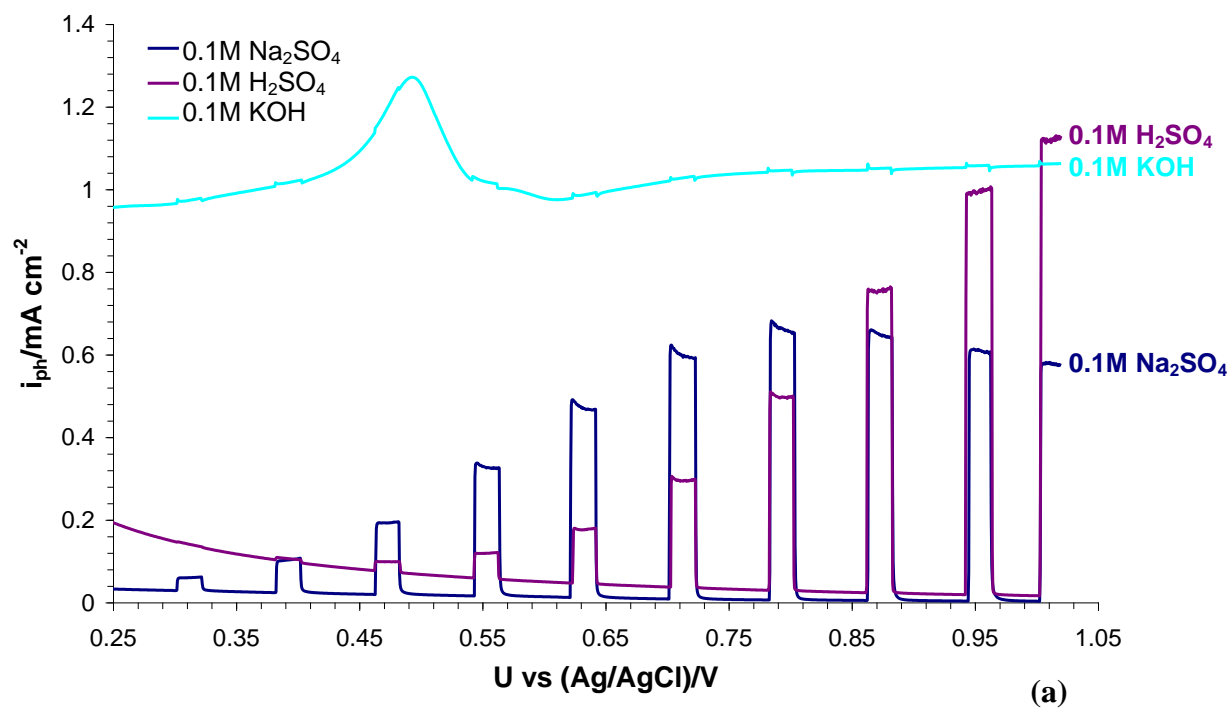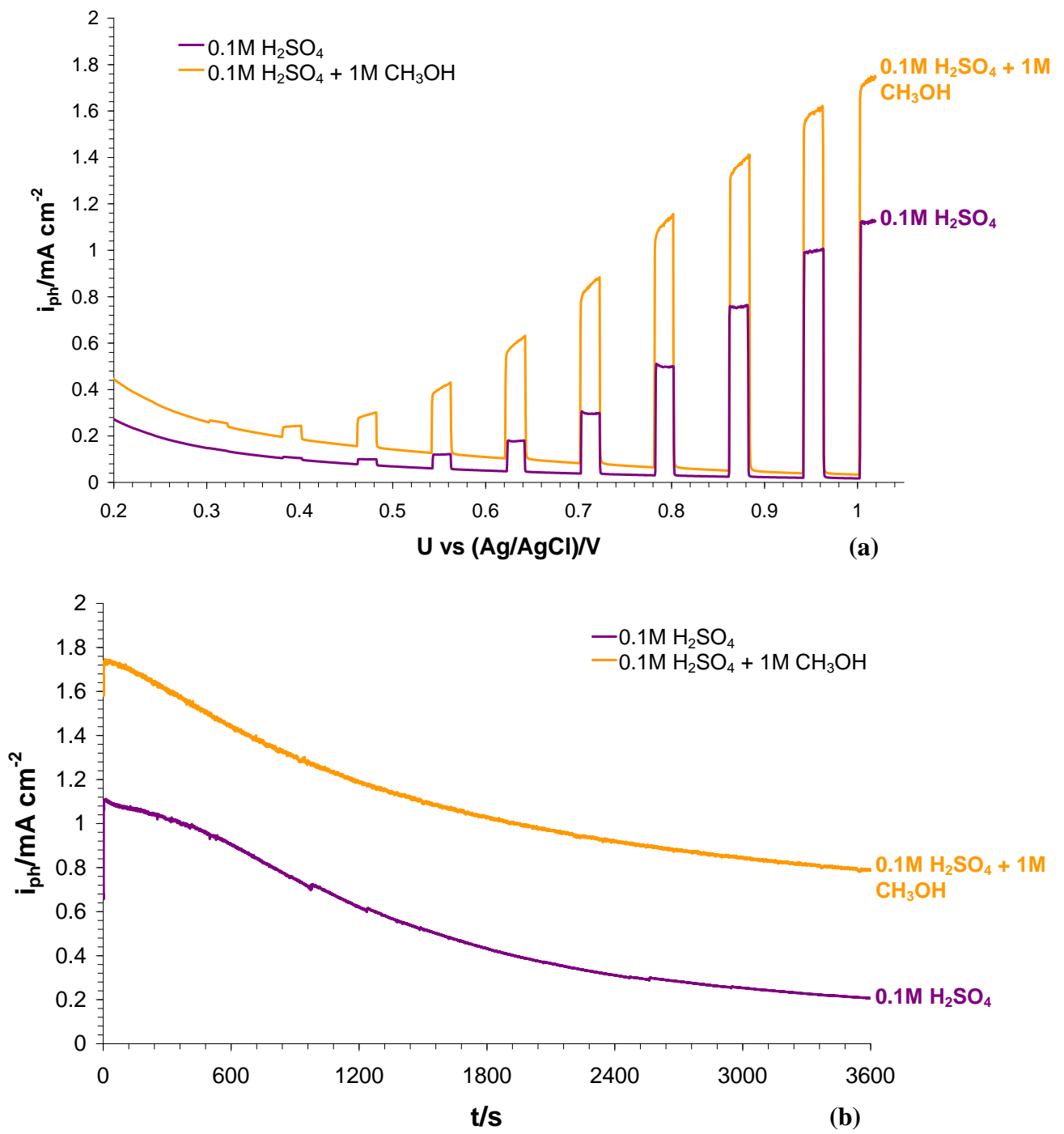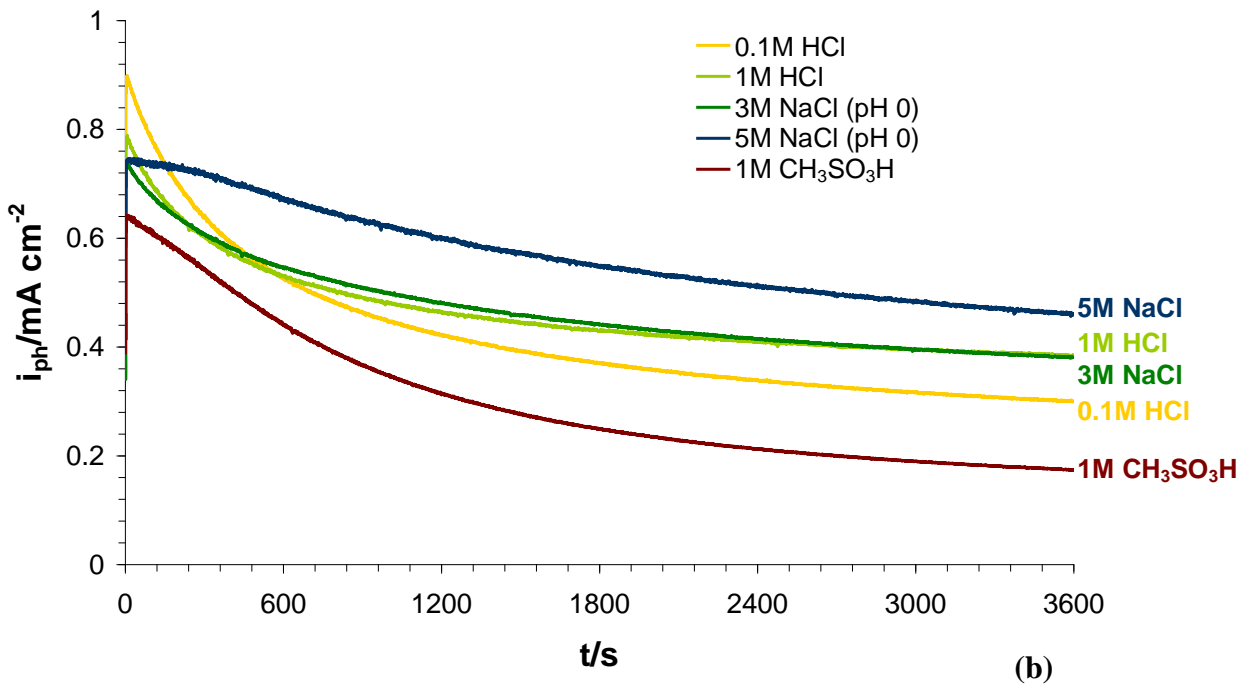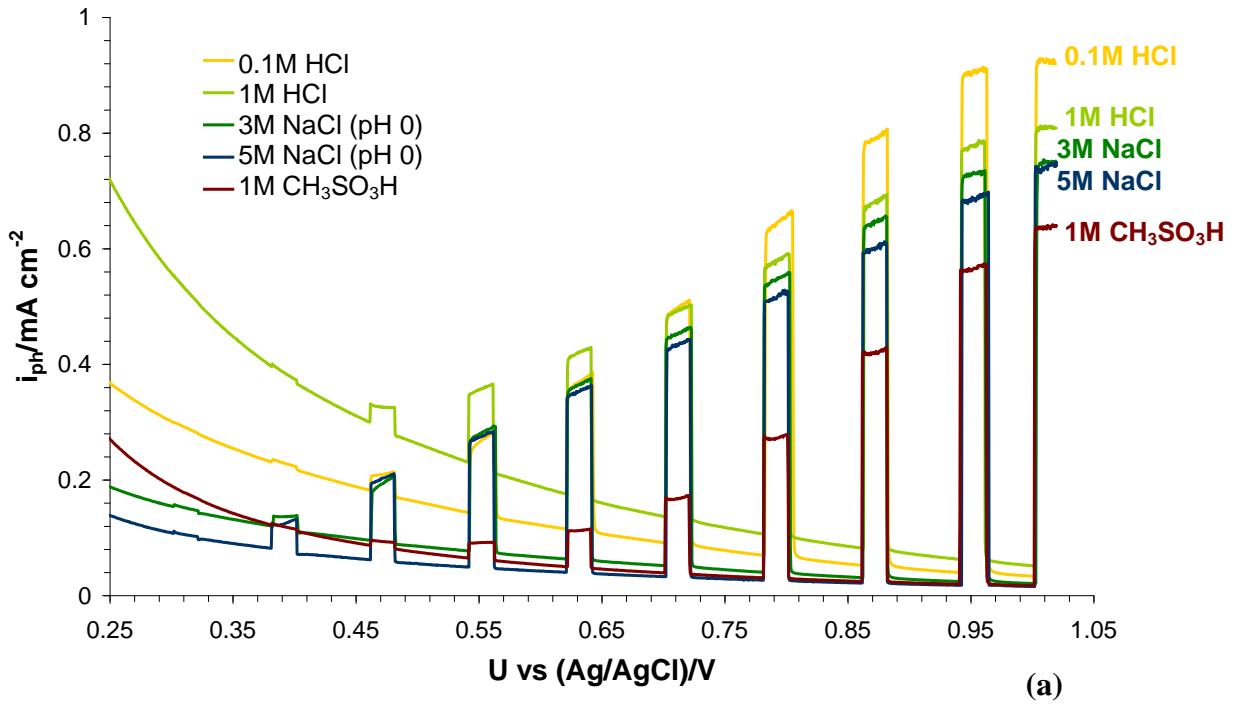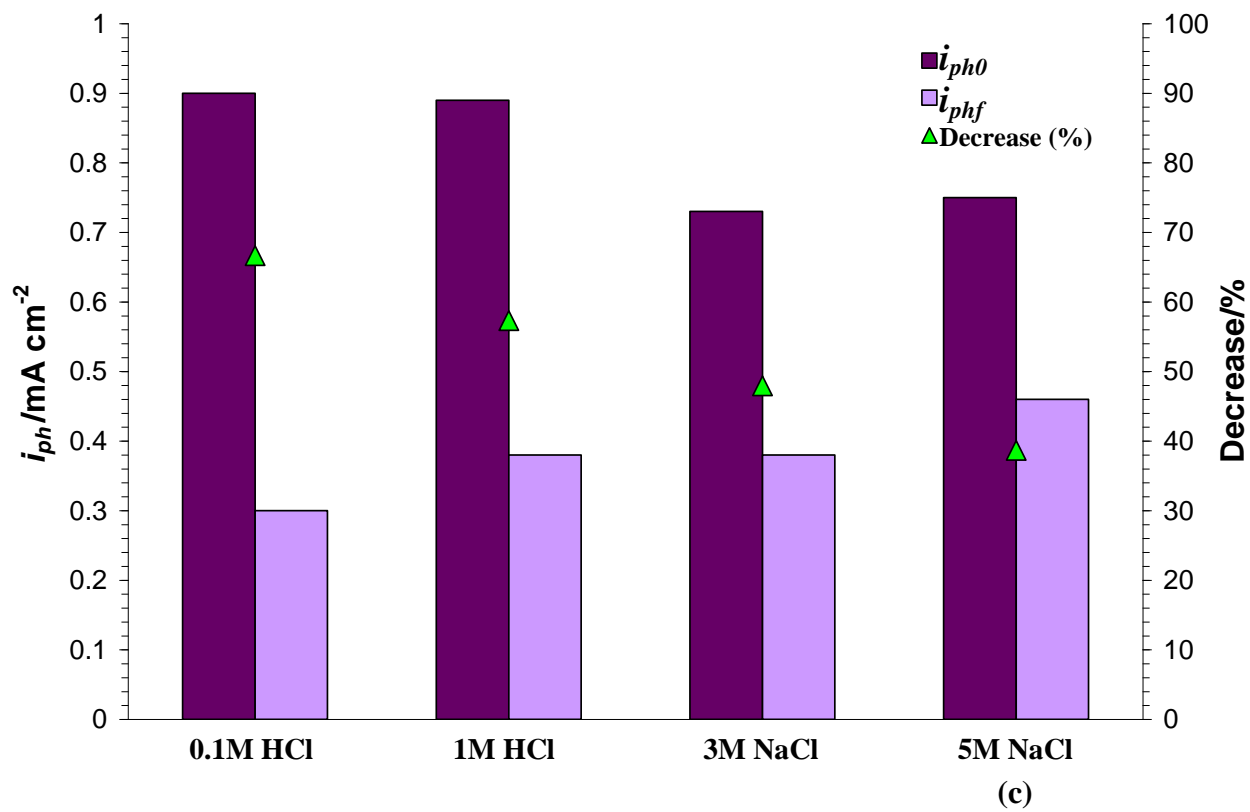
Figure 11

Figure 12

(a)

(b)

(c)
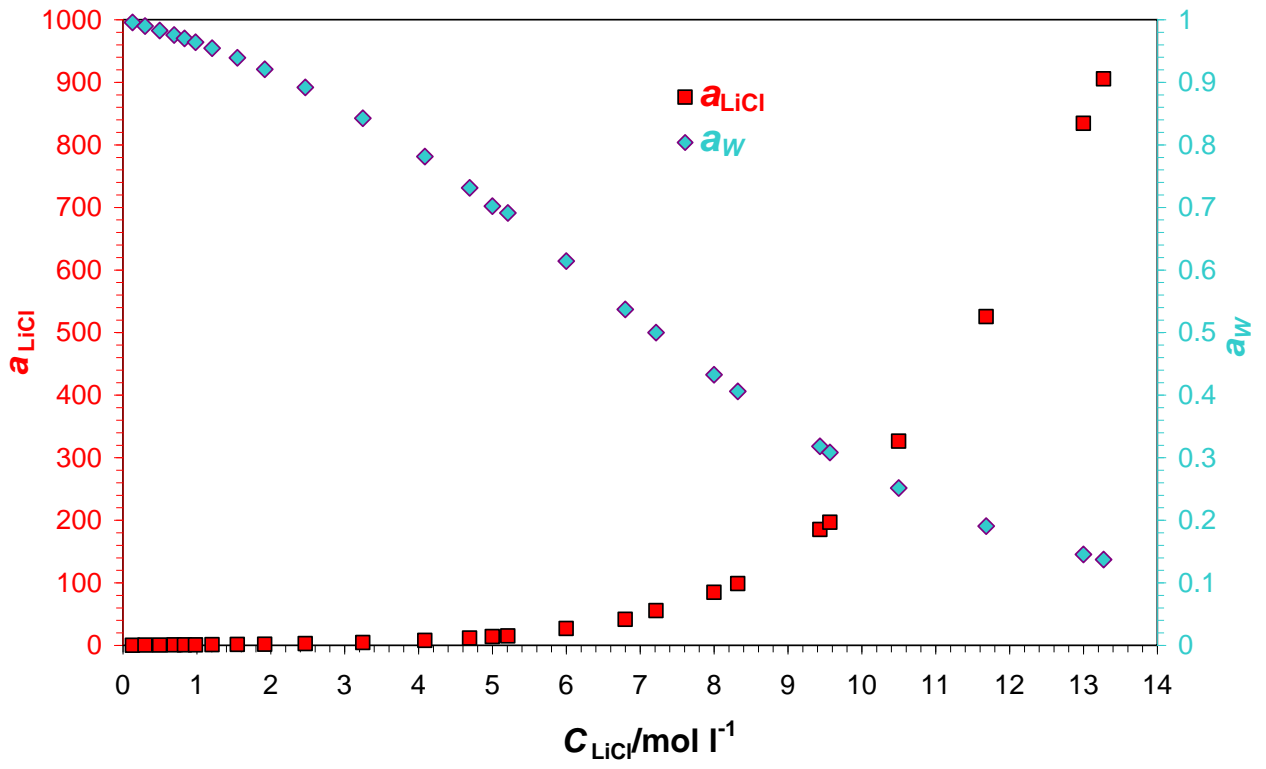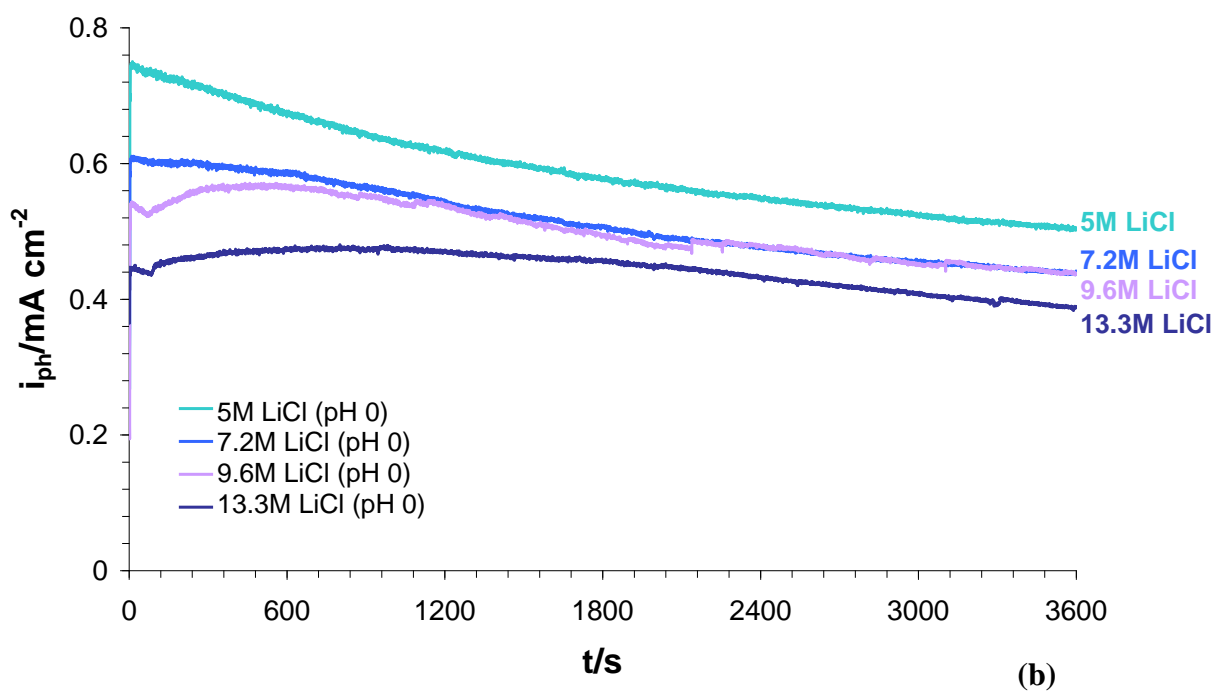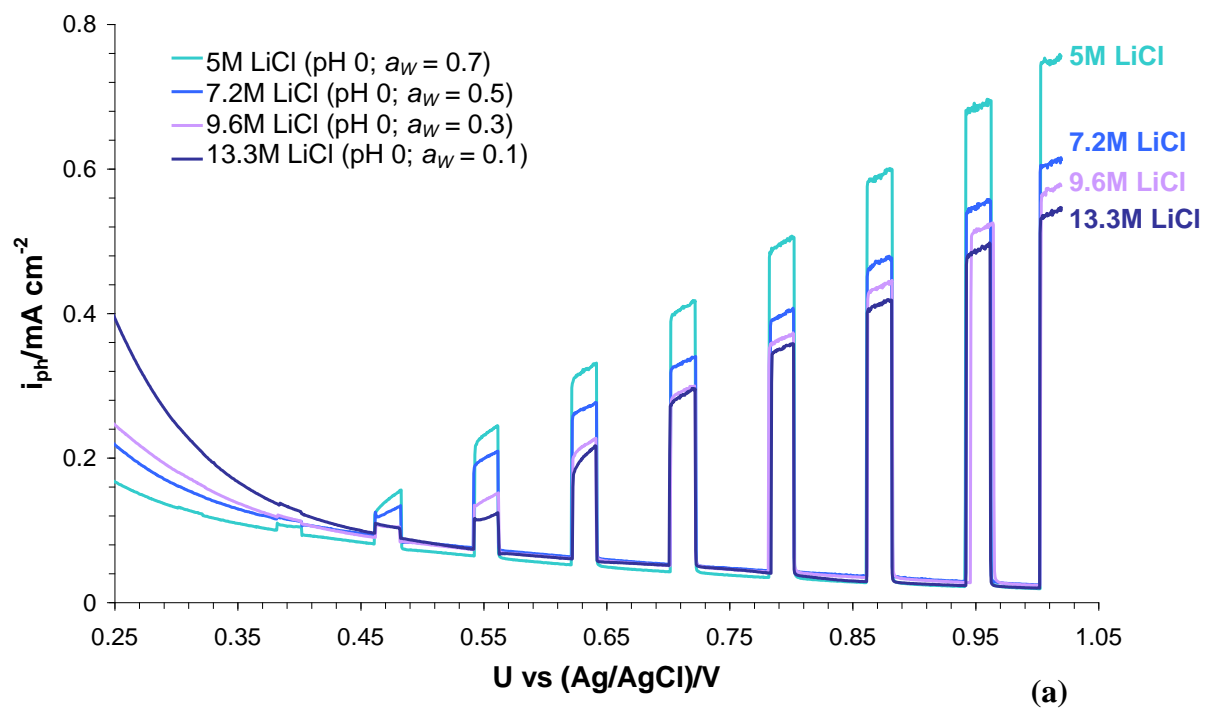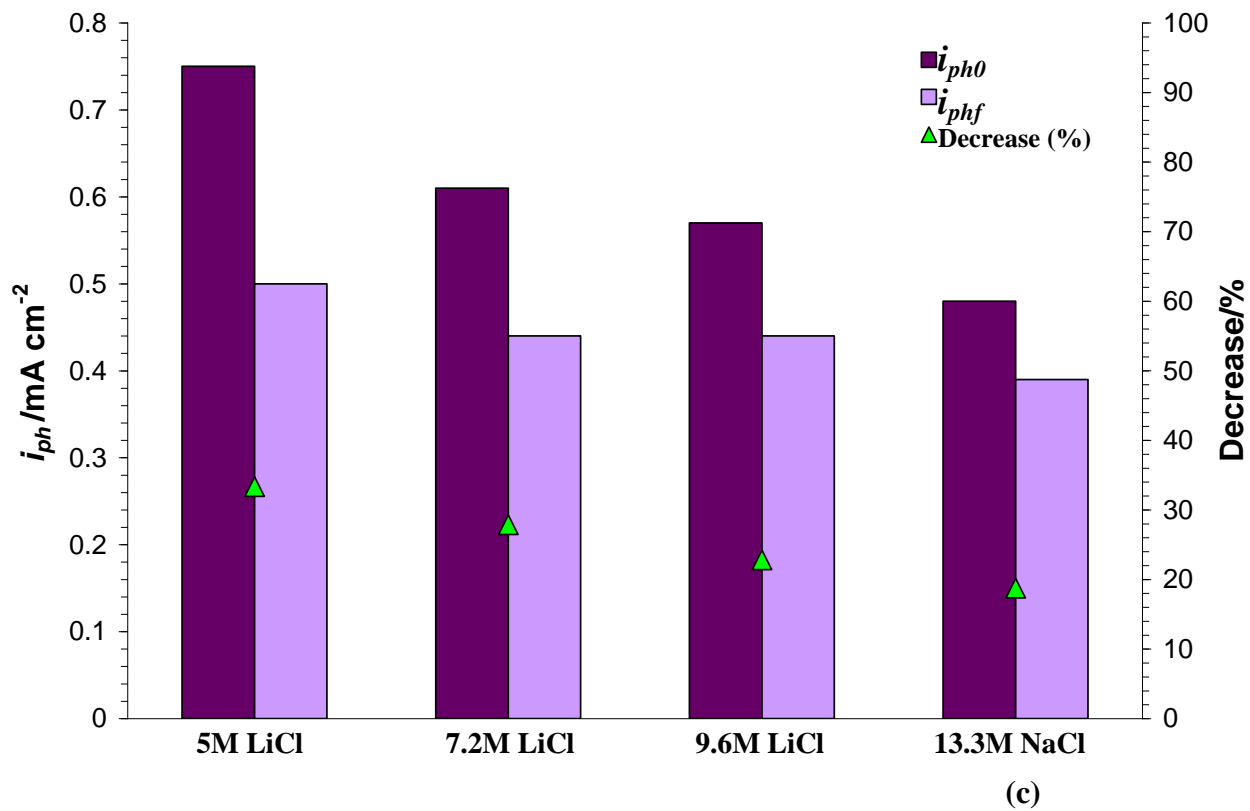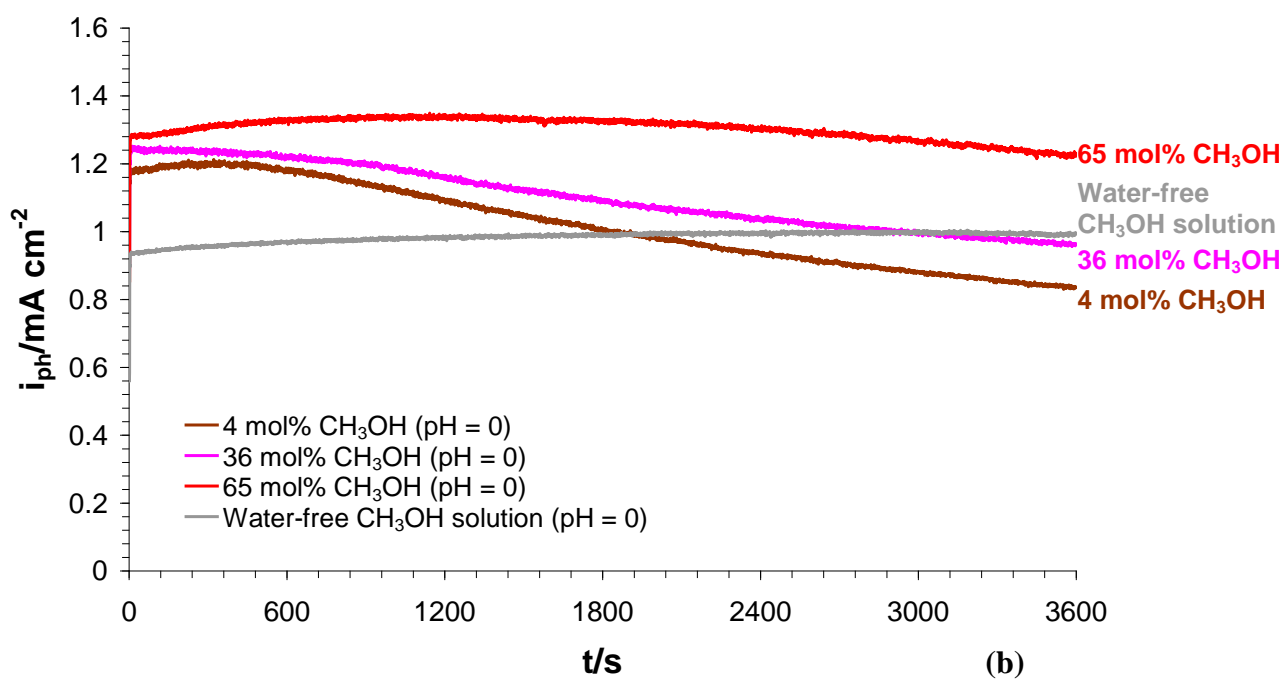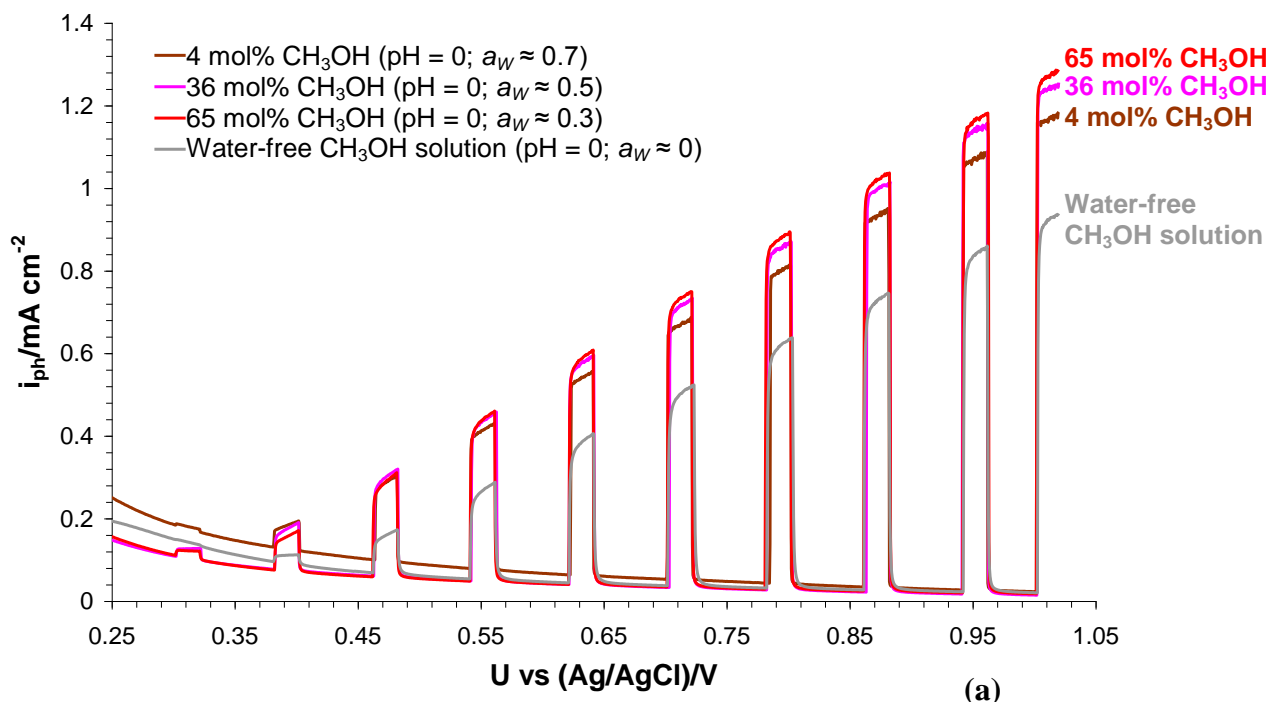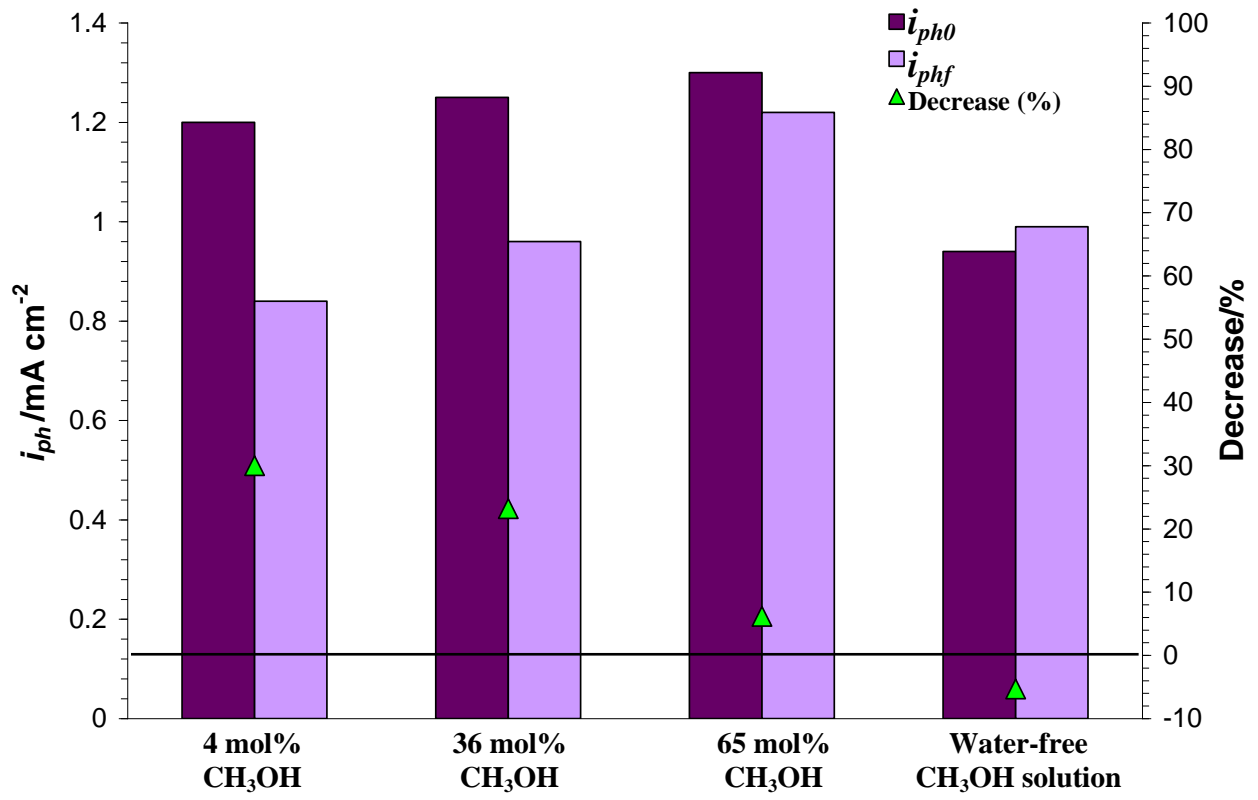
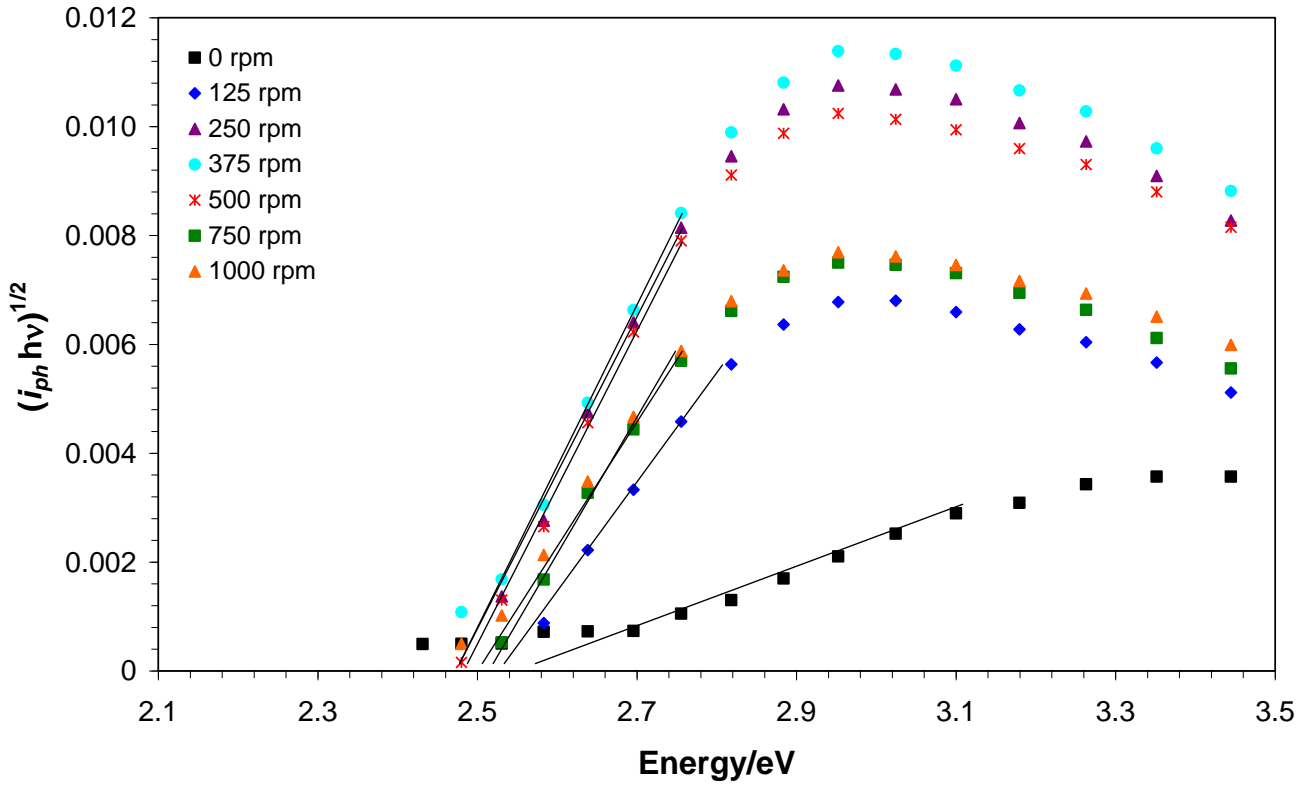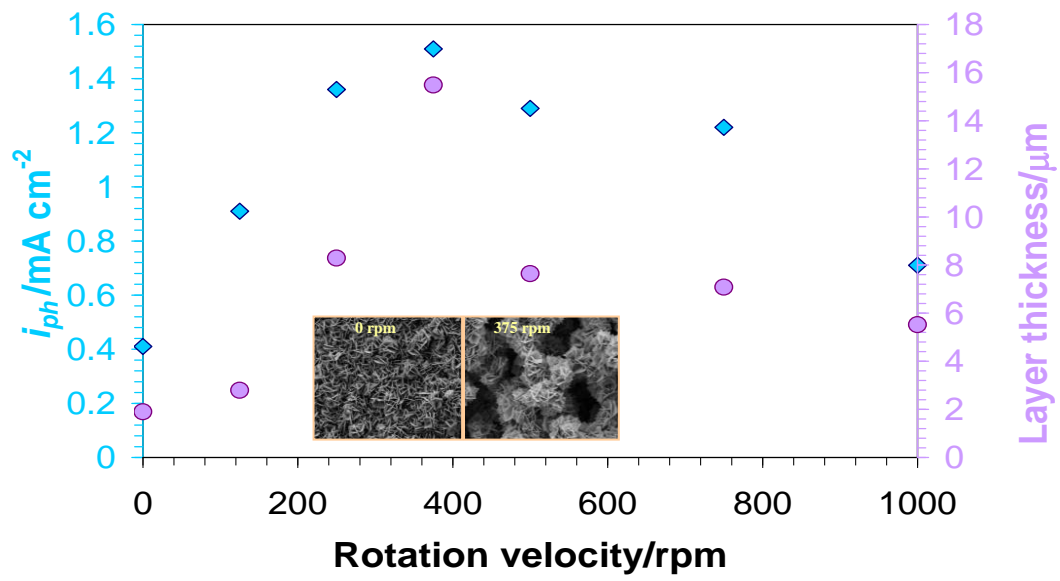**Figure 13**

(c)

Figure 14
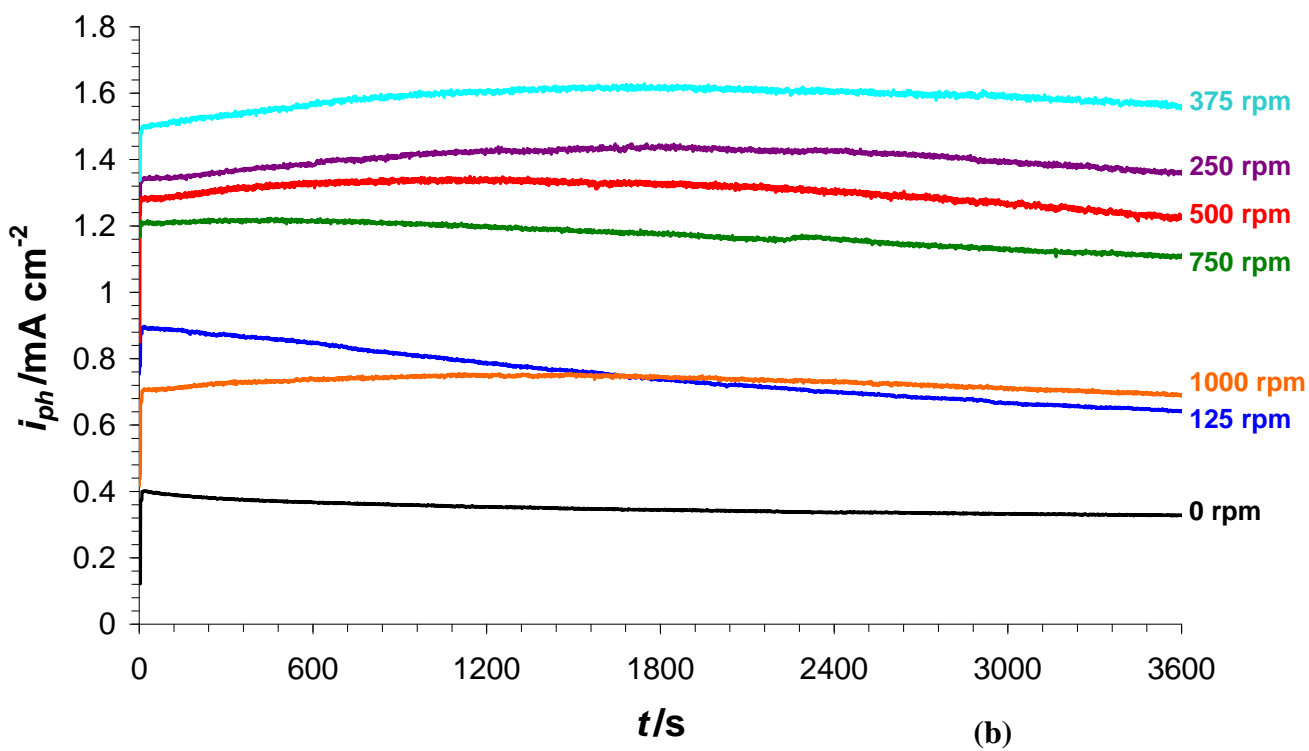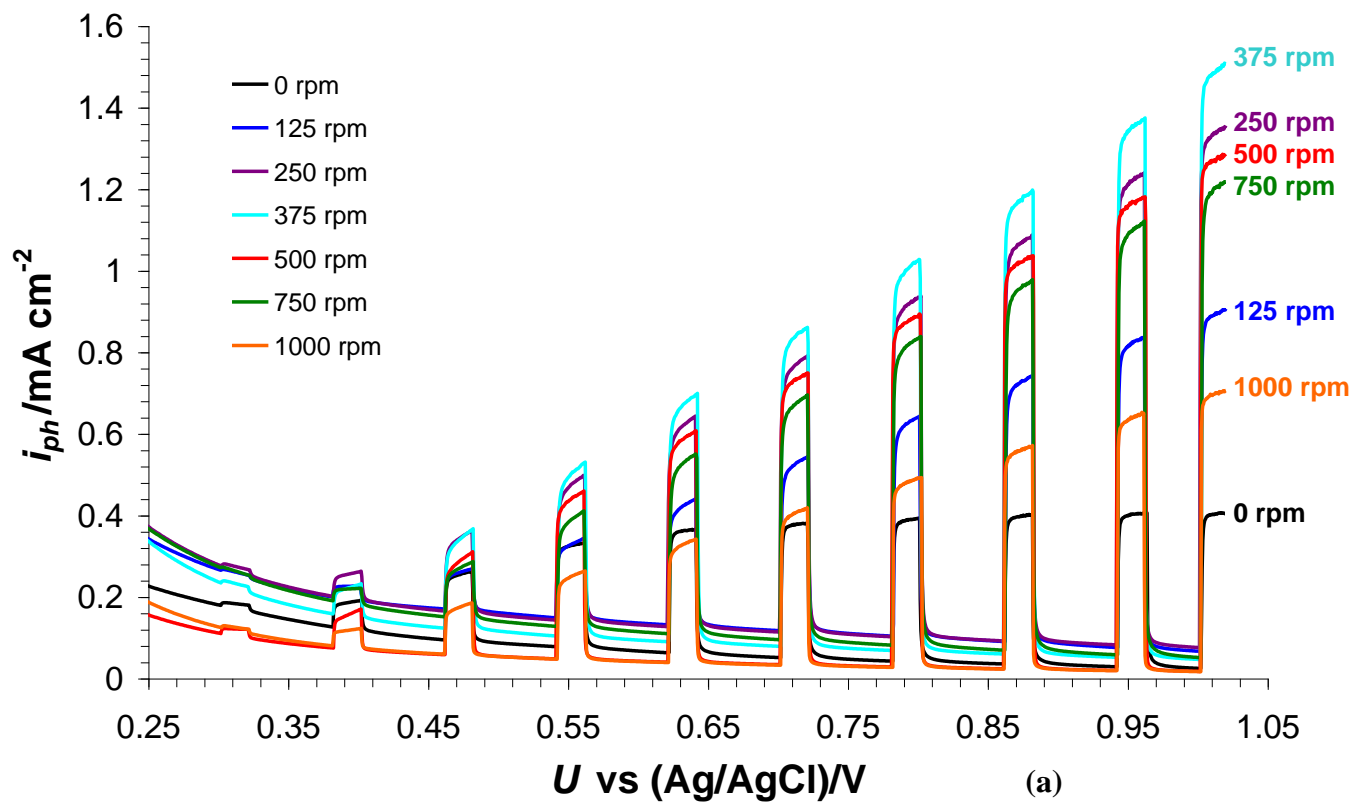
Figure 15

WO$_3$ nanoplatelet globular clusters united in a tree-like fashion were obtained

Influence of rotation velocity (RDE) during W anodization has been investigated

The thickest nanoplatelet layer was obtained at 375 rpm, exposing high active area

At 375 rpm, the charge-transfer resistance decreased, enhancing photocurrent response

Nanostructures were highly stable in aqueous/methanolic mixed solutions with LiCl